

**POLITECNICO DI TORINO**

**Corso di Laurea Magistrale  
in Ingegneria Energetica e Nucleare**

Tesi di Laurea Magistrale

**CFD Analysis of the Cooling Flow in a  
Heavy Industrial Gas Turbine Blade**



**Relatori**

Prof. Mirko Baratta  
Prof.ssa Daniela Misul

**Candidato**

Francesco Cardile

Febbraio 2019

... *Al.*

# Contents

Abstract .....	iii
1. Introduction .....	1
1.1 Future Energy Scenarios.....	1
1.2 Purpose of This Study.....	2
1.3 Outline of the Thesis.....	3
2. Blade Cooling Techniques .....	5
2.1 General Gas Turbine Description.....	5
2.2 Turbine Blades Cooling Schemes.....	7
2.2.1 Convection Cooling.....	9
2.2.2 Impingement Cooling.....	12
2.2.3 Film Cooling .....	13
2.2.4 Steam cooling.....	15
3. <i>EthosEnergy Group</i> Case: TG20B7/8 turbine.....	16
3.1 General Machine Description.....	16
3.2 Row 1 Blade Design Evolution .....	17
3.3 PH4165 Software.....	20
4. Theoretical Preliminaries .....	23
4.1 Governing Equations .....	23
4.2 Finite Volume Method.....	25
4.2.1 Integrals Approximation .....	27
4.2.2 Interpolation .....	28
4.2.3 Iterative Procedure .....	30
4.2.4 Finite Volume Solution Implementation.....	31
4.3 Turbulence Modelling .....	32
4.3.1 Kolmogorov Theory .....	33
4.3.2 Reynolds-Averaged Navier-Stokes Equations .....	35

4.3.3	k-ε Model .....	37
5.	First Case Study: Radial Holes Cooling Channels.....	40
5.1	One Channel Geometry: Grid Independence Study .....	40
5.1.1	Prism Layers Sensitive Analysis .....	41
5.1.2	Polyhedral Meshing: Base Size Sensitive Analysis .....	45
5.1.3	Structured Meshing: Channel Layers and Base Size Sensitive Analysis.....	47
5.1.4	Final Results and Comments on Grid Independence Analysis .....	54
5.2	First Group Geometry.....	57
5.2.1	Steady-state Analysis .....	58
5.2.2	Transient Analysis.....	60
5.3	Fifteen Channels Geometry .....	61
6.	Second Case Study: Ceramic Core Insert.....	68
6.1	Thermal Fluid Dynamic Analysis: Criticalities of the system.....	68
6.2	Segregated Isothermal Analysis .....	70
6.2.1	ANIMA Region Base Size Sensitive Analysis.....	70
6.2.2	Final Results and New Possible Design .....	71
7.	Conclusions .....	73
7.1	Summarizing Conclusions .....	73
7.2	Future Studies .....	74
	Bibliography.....	76

## Abstract

The present thesis work aims to model air flow path inside first row blade of a heavy industrial gas turbine made by *EthosEnergy* Italia (former *FIAT Avio*), using Computational Fluid Dynamic (CFD) analysis. The results are used to validate an inhouse developed software for secondary air flow network modelling, named *PH4165*.

The purpose is to verify modifications that have been done to improve both manufacturability and cooling effectiveness of the first-row blade of the engine called TG20, equivalent name for *Westinghouse* W251. Quartz inserts were used in the old geometry to create ducts during the casting process. Irregular blade shape was causing frequent rupture of the inserts and high amount of casting scraps. A new blade geometry was designed to solve this issue.

A comprehensive fluid dynamic analysis of both blade cooling geometries is presented in this study. Simulations are done using *Star-CCM+*, a commercial software by *CD-Adapco* which is based on Finite Volume Method (FVM). Extended mesh sensitive analysis has been carried out for single cooling channel, proving consistency of the model. These results were used for the complete geometry simulation. Using the best suited interpolant methods, a complete local heat transfer map has been obtained, showing that average heat transfer values estimated from *PH4165* are lower than CFD computed ones.

CFD analysis of the new geometry that has a ceramic insert, is showing that air flow is suffering of stagnation, which leads to a poor heat transfer mechanism between cooling air and blade material.

As a conclusion, results of *PH4165* tool are accurate enough for old blade geometry. However, CFD simulation was necessary in order to highlight some issues in new blade design, that otherwise would have been neglected.

## Sommario

Lo scopo del seguente lavoro di tesi è quello di creare un modello caratterizzante il flusso d'aria all'interno la palettatura del primo stadio di espansione di una turbina a gas di tipo “*heavy industrial*”. La turbina in esame è prodotta da *EthosEnergy* Italia, ex *Fiat Avio*. I modelli numerici impiegati sono basati su analisi fluido dinamiche computazionali. I risultati di tali simulazioni sono impiegati per validare i dati di un software interno dell'azienda, denominato *PH4165*.

L'obbiettivo è quello di verificare le modifiche apportate alla palettatura della turbina chiamata TG20, nome equivalente del modello W251 di derivazione *Westinghouse*. Inserti in quarzo venivano impiegati per creare i condotti interni alla pala durante il processo di manifattura. La forma irregolare della pala era causa di frequenti rotture durante la produzione del componente, determinando un alto numero di scarti di lavorazione. Una nuova geometria è stata quindi adottata per risolvere questo inconveniente.

Nel seguente studio è presente un'analisi esaustiva di entrambe le geometrie di raffreddamento. Le simulazioni sono state svolte usando *Star-CCM+*, un software commerciale per la CFD basato sul metodo dei volumi finiti. Inizialmente è stata svolta l'analisi di sensitività della mesh applicata al singolo canale, provando così la consistenza del modello. I seguenti risultati sono stati poi estesi all'analisi della geometria completa. Impiegando metodi di interpolazione, si è ricavata una mappa completa del coefficiente locale di scambio termico convettivo. Si è provato che i valori stimati col software *PH4165* sono inferiori rispetto ai risultati ottenuti con la simulazione CFD.

Le simulazioni della geometria con inserto ceramico mostra che il flusso soffre di stagnazione, comportando un ridotto rateo di scambio termico convettivo fra l'aria di raffreddamento e il materiale della palettatura.

In conclusione, i risultati del software *PH4165* sono accurati per l'analisi della vecchia geometria di raffreddamento. Al contrario, l'analisi CFD si è dimostrata necessaria per evidenziare alcune problematiche della nuova geometria di raffreddamento, che altrimenti sarebbero state trascurate.

# 1. Introduction

## 1.1 Future Energy Scenarios

Carbon fossil combustion is still today the predominant way to produce electricity all around the world. Although energy production from renewable sources is expected to increase from 25% of total energy production up to almost 41%, still most of the electricity will be produced by carbon fuels in 2040.

According to International Energy Agency prediction [1], it is expected a decrease of installed power capacity of coal and oil fired power plant, with consequent increase of gas and renewable capacity, as reported in [Figure 1.1](#).

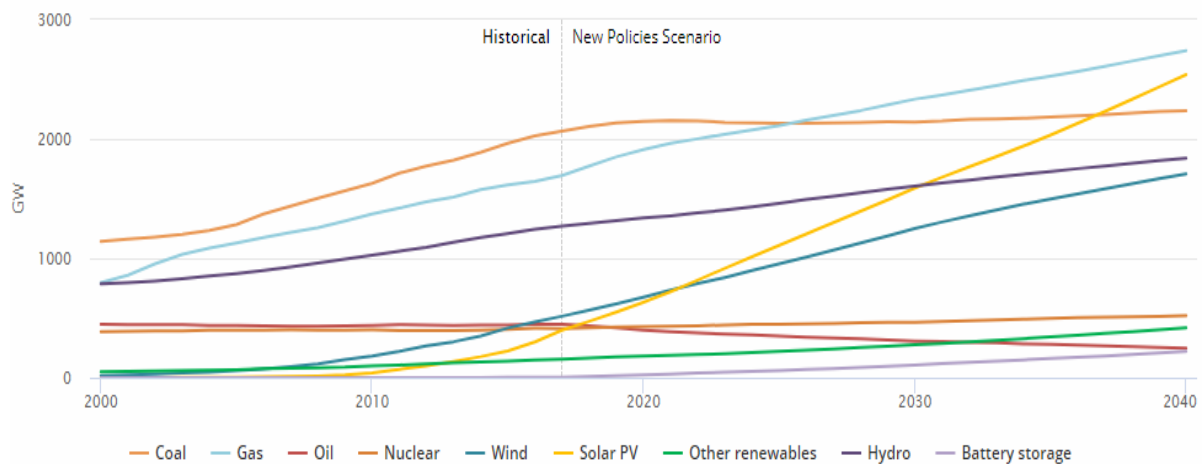


*Figure 1.1: Global installed power capacity, from International Energy Agency (IEA), 2018*

Focusing on gas capacity, it is expected to overtake coal way before 2030 and to become main global energy source in 2040: this is likely due to growing necessity of flexibility in electricity production, as well as necessity to adopt a cleaner energy source in order to achieve environmental standard concerning pollutants emission.

In this context, the main technology for electricity production seems to be the turbo gas machinery: this because of the high-density power, high efficiency, low emissions and high total power plant achievable.

According to experts [2], in the next years a partial decrease of number of units sold per years is expected, as can be appreciated in Figure 1.2. This is because of the overcapacity power generation and consequent decrease of energy price. After that, the number of units sold is going to increase for installation of large combined cycle plants in many industrialized countries of the world, as well as replacement of old units for pollution reason.

Considering these, we can say that interest in gas turbine technology is expected to increase in the upcoming years and the necessity to further develop efficiency of these machines is one of the most challenging goals of the energy sector for the future.

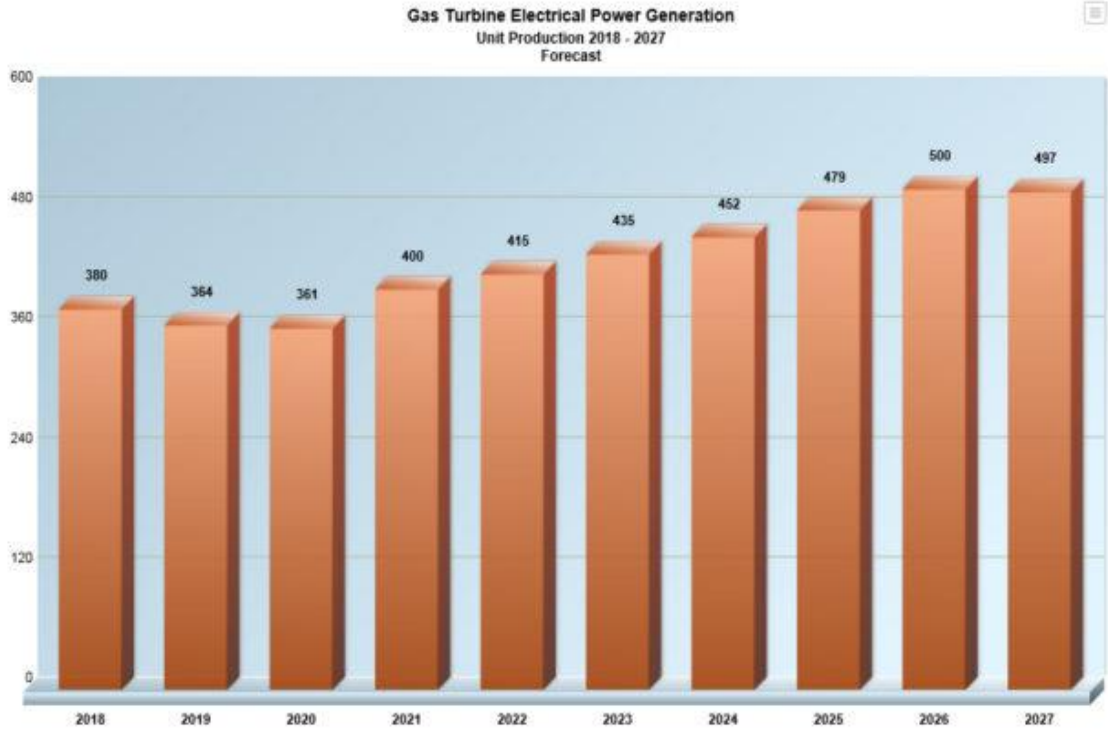


Figure 1.2: Number of turbo-machineries units sold, forecast from International Turbomachinery journal (2018)

## 1.2 Purpose of This Study

This thesis is the result of a collaboration between Politecnico di Torino and EthosEnergy Group, a company specialized in manufacturing components like steam turbines, heavy duty

gas turbines, compressors, generators and other rotating equipment for power generation, industrial and Oil & Gas sector. *EthosEnergy* operates in more than one hundred countries and offers many services for energy sector's components like new build, commercial operation and maintenance, as well as machinery life extension and decommissioning.

As a result of this partnership, students are contributing for developing new technological solutions for many company's products.

This work is focused on setting numerical simulations for testing and validate cooling channels effectiveness in rotor blades of the TG20B7/8 gas turbine. This 48 MW machine is from Fiat turbo gas division and was developed starting from Westinghouse W251 project. The TG20 turbine has experienced many technical revision and update from its initial project (1959), like compressor redesign, new coating surfaces and new combustion system for NOx emission reduction.

One of the latest updates (2017) was the modification of casting procedure for rotor blades of the first vane of the turbine section, with consequent modification of the geometry of cooling path inside the turbine blades. Engineers from *EthosEnergy* predicted consequences of this modification using the *PH4165* software, a Fortran environment based calculator for estimation of complex air flow network inside the turbine but, considering the limitation of this software, they wanted to validate these results with the Computational Fluid Dynamic (CFD) tool.

In order to do that, starting from 3D models of the cooling path inside TG20 rotor blade, many numerical simulations have been set in order to calculate most important physical parameters of internal air flow, as well as heat transfer coefficient of the system. All the simulations have been developed with *Star-CCM+* software from *CD-Adapco*.

### 1.3 Outline of the Thesis

This work is subdivided in 7 chapters: in [Chapter 1](#) a presentation of context and motivations of this work have been presented. In [Chapter 2](#) we will give a general description of turbo gas technology and which are the main cooling schemes for rotor blades in modern turbomachinery. In [Chapter 3](#) the TG20 case will be presented, with general description of the machine and motivations behind the choice to change casting procedure for the row #1 rotor blade. This will also give us the possibility to present the *PH4165* software, how does it work, its main limitations and results obtained from it.

In [Chapter 4](#) all the governing equations describing the air flow physics will be presented. Moreover, a general description of the Finite Volume method (FV) will be given, which is the numerical scheme adopted by *Star-CCM+* software. Then a brief presentation of turbulence models, closure problem and a resume of k- $\epsilon$  model, which is the one adopted in all the simulations.

In [Chapter 5](#) we will finally present the numerical simulations of old cooling geometry (“radial holes”) and the results obtained from them. This study has been developed starting from the simplest case (analysis of single channel), then it has proceeded with the analysis of a subset of the domain of interest and, in the end, results of the analysis with all the cooling channels of the rotor blade are presented.

In [Chapter 6](#) results of currently adopted cooling geometry will be presented and there will be also a comparison of cooling effectiveness between two geometries.

Conclusion of this study is in the [Chapter 7](#), with a resume of the entire work, comments on results from simulations and suggestion for possible future studies.

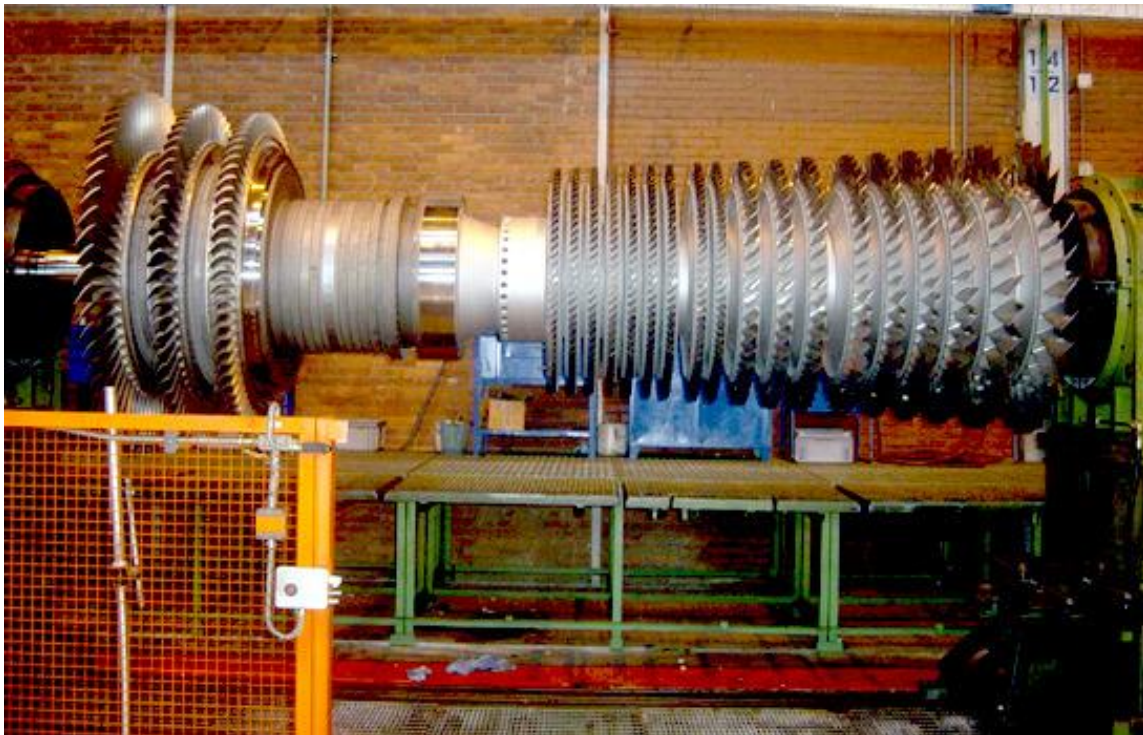


*Figure 1.3: TG20B7/8 turbine, courtesy of EthosEnergy group*

## 2. Blade Cooling Techniques

### 2.1 General Gas Turbine Description

A gas turbine is a rotating turbomachinery in which working fluid is a compressible one, usually air. This machine is used for electricity production as well as propulsion of planes, ships, trains, and other vehicles. We can consider the thermal cycle reported in [Figure 2.1](#) to explain how it works.

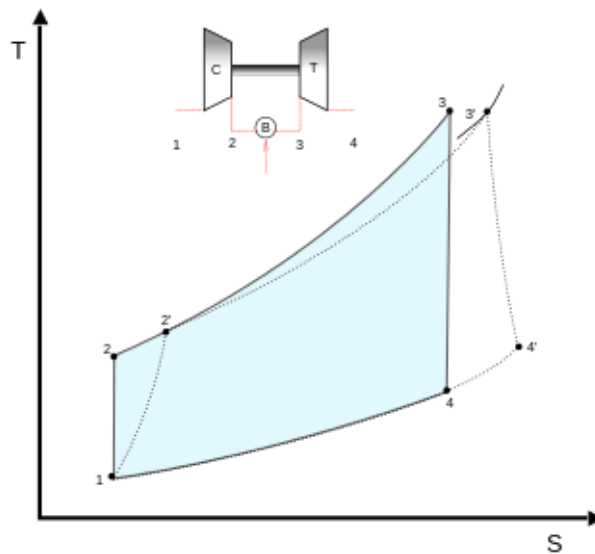


*Figure 2.1: Theoretical (continuous line) and real (dashed line) Brayton – Joule cycle, single shaft gas turbine (source: Wikipedia).*

Reference cycle is called Brayton-Joule cycle: air is extracted from environment at ambient condition (pt. 1) and then it's compressed inside turbo compressor section of the machine: air's temperature and pressure increase (pt. 2). Then the compressible fluid is mixed with a gas fuel and the mixture burns with consequent temperature increase (pt. 3). Hot gases are expanded inside turbine section of the machine and ejected in the environment (pt. 4). The cycle represented in figure is open one, so 4-1 transformation is a fictitious transformation used to have a closed loop. Real Brayton-Joule cycle is presented in [Figure 2.1](#): it takes into account

irreversibility production during compression and expansion, as well as pneumatic losses inside the burner ( $\eta_b < 1$ ) with a consequent pressure decrease ( $p_3 < p_2$ ).

The difference between mechanical work produced by the turbine and absorbed by compressor is positive, so we have net mechanical work production that can be used to generate electricity if gas turbine's shaft is coupled with a turbo alternator.

We define *compression ratio* the ratio between pressures at outlet and inlet section of the compressor:

$$\beta_k = \frac{p_2}{p_1} \quad (2.1)$$

It can be demonstrated that, for an ideal cycle, efficiency is just depending on compression ratio according to the equation (2.2):

$$\eta_{ideal} = 1 - \frac{1}{\beta_k^{\frac{\gamma-1}{\gamma}}} \quad (2.2)$$

Where  $\gamma$  is the ratio between heat capacity at constant pressure and heat capacity at constant volume.

Irreversibility are introduced in the real cycle, so we consider an *adiabatic efficiency* for compressor ( $\eta_k$ ) and turbine ( $\eta_t$ ).

Following assumptions are made:

- Heat capacity of air equal to heat capacity of hot gases after the burner;
- Fuel mass flow negligible;
- No pneumatic losses in the burner.

In this case, real cycle efficiency is expressed as following [3]:

$$\eta_{real} = \left(1 - \frac{1}{\beta_k^{\frac{\gamma-1}{\gamma}}}\right) \left( \frac{\eta_t TIT - \frac{T_{amb} \beta_k^{\frac{\gamma-1}{\gamma}}}{\eta_k}}{TIT - T_{amb} - \frac{T_{amb} \beta_k^{\frac{\gamma-1}{\gamma}}}{\eta_k}} \right) \quad (2.3)$$

Compression ratio ( $\beta_k$ ) as well as Turbine Inlet Temperature (TIT) are both affecting efficiency of real cycle, as can be appreciated in [Figure 2.2](#).

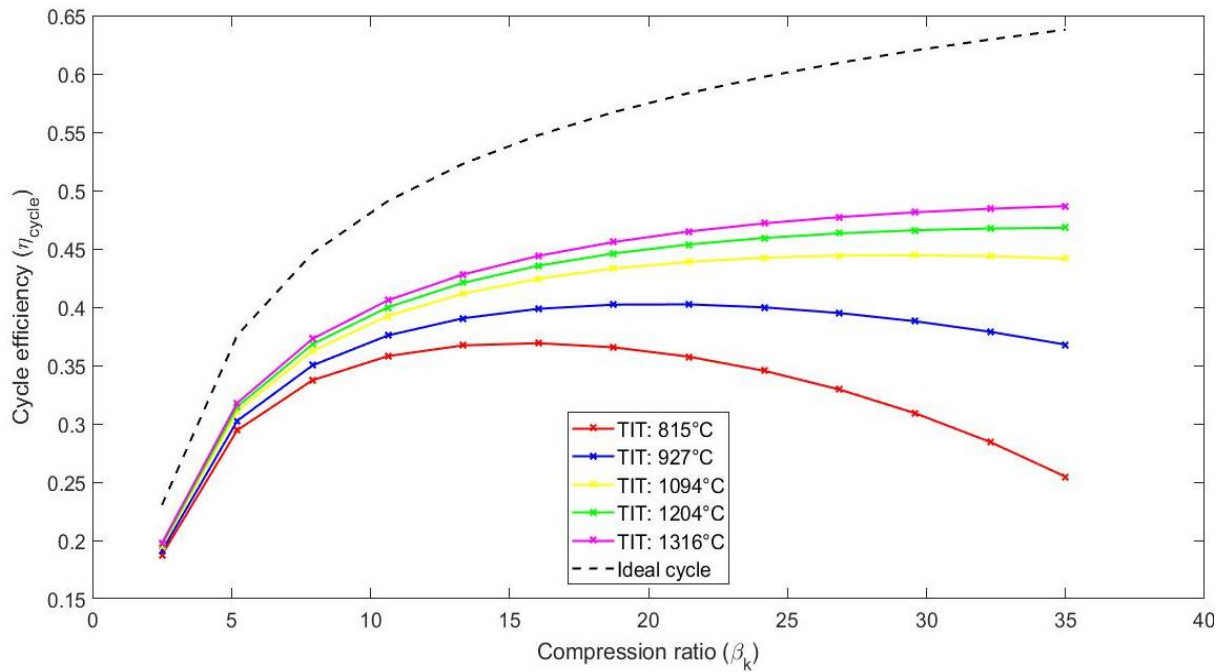


**Figure 2.2:** Theoretical and real cycle efficiency as a function of compression ratio,  $T_{amb}=15\text{ }^{\circ}\text{C}$ ,  $\gamma=1.4$ ,  $\eta_t=0.92$ ,  $\eta_k=0.87$ .

In real cycle case, for excessive high values of compression ratio, efficiency decreases and for each TIT, optimal value of compression ratio can be calculated. Compression ratio is affecting machine dimension: regarding that for axial compressor we have just  $\beta = 1.2 \div 1.3$  compression ratio per stage [4], increasing  $\beta_k$  means also to have higher number of stages, thus length of the machine increases. Moreover, metallurgic limit of gas turbine components is another factor that affect pressure ratio maximum value.

On the contrary, Turbine Inlet Temperature is not affecting machine's size and looking at [Figure 2.2](#) it can be noticed that, for a given pressure ratio, cycle efficiency increases if TIT assumes high values. Thus, theoretically speaking, higher TIT is required in order to have better performance of the gas turbine.

## 2.2 Turbine Blades Cooling Schemes

Firing temperature can't exceed threshold values depending on material properties. Many turbine components are sensitive to high temperature of hot gases from combustor, but rotor blades of first expansion stage are the most exposed to thermo-mechanical stresses and usually

are the limiting one. Since 1950, technical research has been devoted on developing new turbine bucket materials with higher temperature capability, but also cooling system for stator and rotor blades has been introduced. In order to reduce metal temperature, air is bled from compressor stages and it is sent to stator, rotor, casing and other parts of the turbine.

During the last 60 years, gas turbines experienced firing temperature increase as new and more effective cooling techniques has been introduced [5].

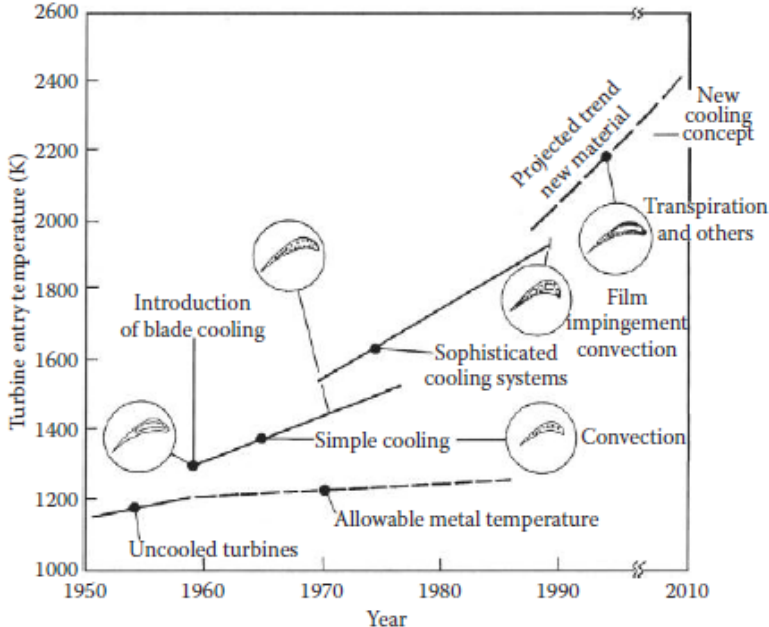


**Figure 2.3:** Variation of turbine entry temperature over recent year, from Lakshminarayana B.: “Fluid Dynamics and Heat transfer of Turbomachinery”. Chapter 7, pp. 597–721.1996. Copyright Wiley-VCH Verlag GmbH & Co. KGaA.

There are three main mechanisms adopted for turbine blade cooling in modern gas turbine: these are combined in order to obtain best performance achievable. In Figure 2.4 is presented a state of art solution for blade cooling [6]: air stream flows from rotor disc and gets into a structured cooling path, with many air bleeding and ramification. Inlet section of cooling air is located in blade’s root – pressure side, then coolant is forced to proceed along a serpentine, from blade’s leading edge to trailing edge. Also some air bleeding is located in leading edge region, in order to have local cooling thanks to *shower head* technique (2.2.2). Cooling of mid-chord region may also be enhanced by angled rib turbulator (2.2.1). Proceeding along the path, air reaches the trailing edge region, where part of the air is extracted from the main flow in order to cool-down by film cooling technique this region. Remaining air is forced to proceed

along the serpentine, following a specular path, in order to cool down the suction side (see cross section image of [Figure 2.4](#)): in this case, less mass flow coolant is needed because usually suction side thermal load is less than pressure side. In the end, remaining air is ejected from tip of the blade, also in order to increase rotor's torque.

Next part of the thesis will be dedicated to a brief presentation of the three typical blade's cooling mechanisms adopted in modern gas turbine. It is worth also to include steam cooling, because thanks to this technique it is actually possible to achieve highest firing temperature.

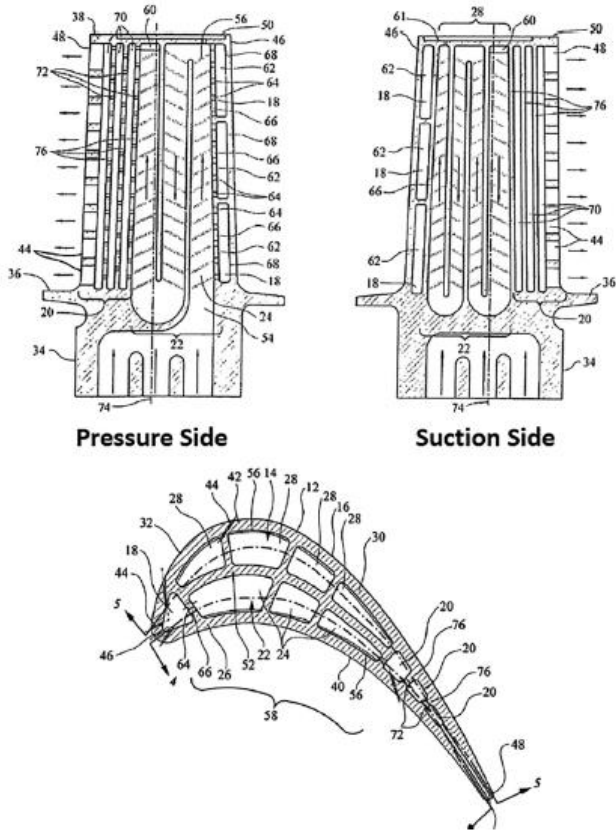


*Figure 2.4: Bifurcated blade with serpentine passage design, from J.Town et al.: "State-of-the-Art Cooling Technology for a Turbine Rotor Blade" (201, pp. 6).*

### 2.2.1 Convection Cooling

Cooling air is flowing inside turbine's blades trough channels, so heat is removed thanks to wall interaction with coolant. Usually, cooling stream is radial, so air is flowing from root of the rotor blade to the tip.

Air path may be just a straight channel, as in the case of *radial holes* cooling channel geometry, or a more complex serpentine, in which air is forced to make multiple passages from hub of the blade to the tip ([Figure 2.5](#)) and increase heat exchange surface, paying higher pressure drop. Effectiveness of convection cooling may also be increased using various 2D turbulence promoter. One example is the rib turbulator, consisting of internal fins that determines detachment of the fluid at rib's tip and reattachment in the spacing between one rib and the successive one ([Figure 2.6](#)): in this way turbulence is increased and local value of Nusselt number is higher with respect to a smooth channel [7]. Ribs may be present on both opposite walls of square shaped duct, or just one side, facing the most critic surface of the air foil (load on pressure side is typically different between the one in suction side).

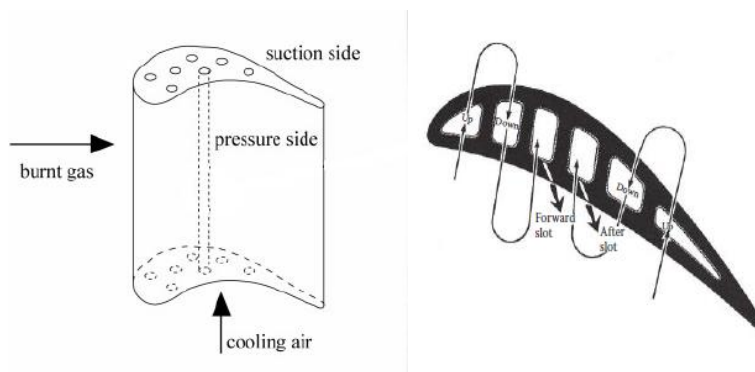


**Figure 2.5:** Examples of “radial holes” cooling geometry (left, from “Real time numerical simulation and visualization of electrochemical drilling” by Alexandru Telea) and cooling system with two three-pass serpentine (right, from Halila, E.E. et al., *Energy efficient engine*, General Electric Company, Fairfield, CT (prepared for NASA CR-167955), 1982.)

Many studies have been carried on in order to find optimal rib turbulator configuration, in particular:

- Shape of the rib (square, rectangular, semi-circular, ...) and its aspect ratio;
- Rib's orientation with respect to air flow main direction (transverse, downstream angled, upstream angled, spiral angled, ...);
- Correct spacing between one rib and the next one;
- Ribs position with respect to channel's walls.

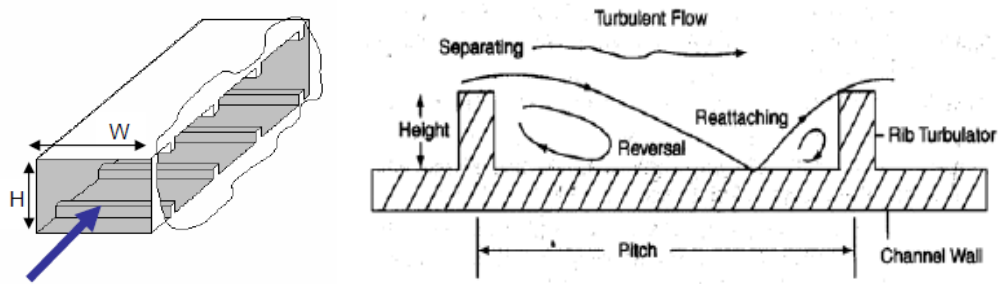


**Figure 2.6:** Schematic of ribbed rectangular channel (left) and flow around a rib(right), from J. Sundberg: "Heat Transfer Correlations for Gas Turbine Cooling" (2006, pp. 11)

Another tool used for 2D turbulence promotion is pin-fin: flow around circular pins is analogous of a flow around a circular obstacle. This technique is adopted in narrow blade's region, where ribs cooling can't be adopted (typically, trailing edge of the rotor blade) [8].

As the coolant flows past the pin, the flow separates and eddies are shed downstream of the pin. Many parameters have must be taken into account in order to optimize fin cooling enhancement; like shape, dimension, spacing, pin array distribution, and others.

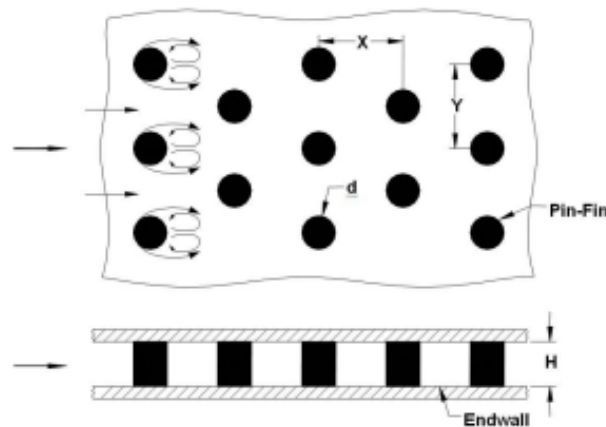


**Figure 2.7:** Example of cylindric obstacles used in pin-fin cooling technique, from S. Gupta1, A. Chaubel et al.: " Review on Heat Transfer Augmentation Techniques: Application in Gas Turbine Blade Internal Cooling" (2012, pp. 59).

## 2.2.2 Impingement Cooling

Impingement cooling is basically a high intensity form of convection cooling: air is boosted towards inner walls of the air foil as a jet stream. With this technique it's possible to have great capability of heat removal in most critical area. Paying a less structural integrity of the blade, jet nozzles can be located in special area like the leading edge of the air foil, where thermal load is high but material thickness is sufficient for locating impingement cooling. Jet flow is obtained thanks to high pressure air, flowing through holes of a perforated surface called *jet plate*, and hitting a target surface, that is consequently cooled down.

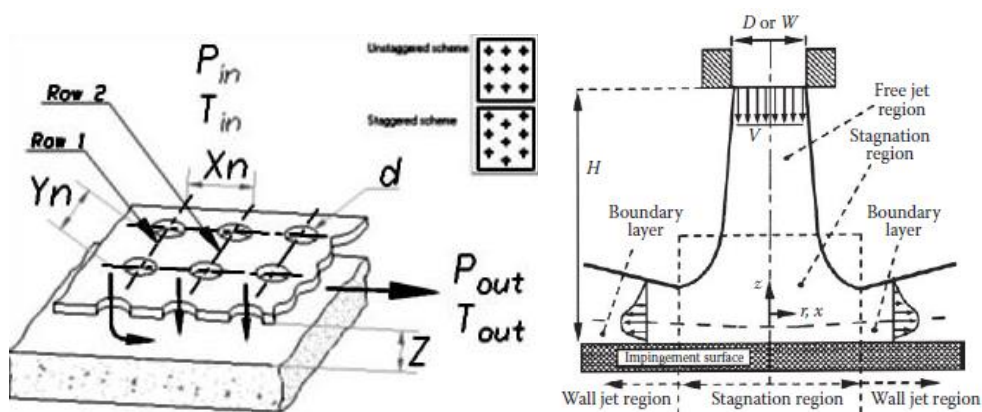


*Figure 2.8: Typical impingement set-up (left) and jet impact on a wall (right), from S. Gupta, A. Chaube et al.: "Review on Heat Transfer Augmentation Techniques: Application in Gas Turbine Blade Internal Cooling" (2012, pp. 65-66).*

Where the jet hit the target, the boundary layer is very thin and the flow is highly turbulent, with a local increase of heat transfer coefficient. Target plate may be flat or curved: the first case is typical in the case impinged surface is in the mid-chord region, the second in leading edge. In this last case, if impingement cooling is combined with film cooling (see [2.2.3](#)) we talk about *shower head* treatment. Many parameters may affect effectiveness of impingement cooling, like jet to target spacing, holes spacing and distribution in jet plate, shape and dimension of the holes, target plate shape, and others. In most advanced design, jet is combined with rib turbulators located in the target plate, to increase vorticity.

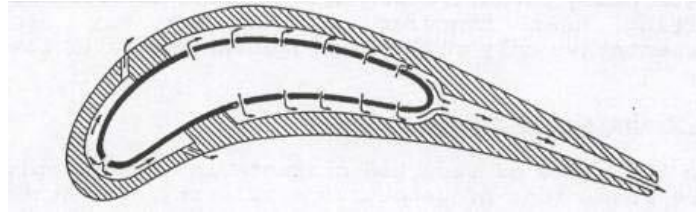


**Figure 2.9:** Example of impingement cooling on inner blade surfaces, from S. Gupta1, A. Chaube1 et al.:” Review on Heat Transfer Augmentation Techniques: Application in Gas Turbine Blade Internal Cooling” (2012, pp. 66).

### 2.2.3 Film Cooling

With this technique, cooling is achieved creating with working air a protective film between hot gases from combustor and rotor turbine blade. Air is extracted from inside the rotor blade and ejected out through discrete holes, creating a thin layer around the air foil that protects the metal surface. In this way, blade is directly protected from overtemperature; on the contrary, internal cooling achieves metal’s temperature reduction thank to wall interaction between inner blade surfaces and refrigerating fluid.

[Figure 2.10](#) shows the heat transfer model associated to film cooling: without film, heat flux to load blade surface is given by:

$$q''_0 = h_0 (T_g - T_w) \quad (3.1)$$

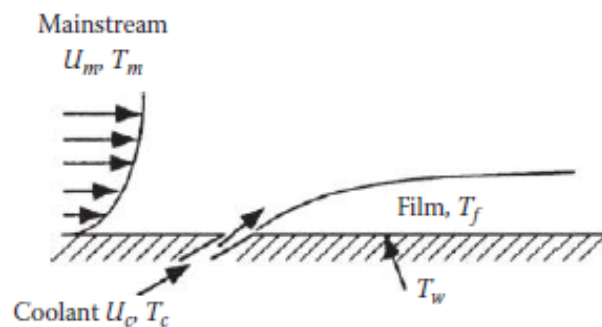


**Figure 2.10:** Schematic of film cooling concept, from J.C.Han and S.V. Ekkad “Recent development in turbine blade film cooling” (1998).

Where  $h_0$  is heat transfer coefficient between hot gases at temperature  $T_g$  and wall at temperature  $T_w$ .

With fluid ejection from holes and protective film formation, new heat flux load is given by:

$$q'' = h (T_f - T_w) \quad (3.2)$$

Film temperature is depending on coolant and hot gases temperature. Heat transfer mechanism is different, so a new coefficient  $h$  will characterize the phenomenon.

Film cooling effectiveness is realized if heat flux ratio is less than 1:

$$\frac{q''}{q''_0} = \frac{h (T_f - T_w)}{h_0 (T_g - T_w)} = \frac{h}{h_0} \left\{ 1 - \eta \frac{T_g - T_c}{T_g - T_w} \right\} \quad (3.3)$$

Where  $\eta = (T_g - T_f)/(T_g - T_c)$  parameter is called *film effectiveness*.

Film cooling may be needed in many locations along the surface of the first row blade, as is showed in [Figure 2.11](#): coolant ejection is located on both leading (*shower head*) and trailing edge as well as pressure and suction side of the blade. Film cooling affects air foil aerodynamic and it could also decrease thermodynamic internal efficiency of the turbine, but usually higher TIT makes up for internal efficiency decrease and overall gas turbine efficiency increases.

Film formation and its effectiveness is a complex subject, and many articles are devoted to explore this important cooling mechanism in modern turbines rotor blades.

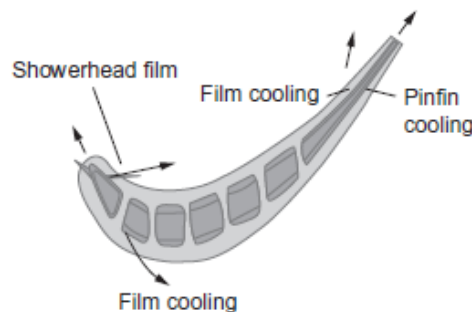


*Figure 2.11: Rotor blade section with film cooling detail, from M.P. Boyce "Gas Turbine Engineering Handbook" (2012, pp. 417).*

### 2.2.4 Steam cooling

If turbine gas machine is part of a combined-cycle plant, water may be considered as coolant. Steam is extracted from HP section of the turbine and sent to hot surfaces of gas turbine machine. Rotoric and statoric surfaces are cooled and steam experiences over-heating before being re-injected in IP section: total plant benefit efficiency increase. In [Figure 2.12](#) an example of steam-cooled rotor blade is showed: a certain number of channels are embedded inside the turbine blade in order to have steam flow, heat transfer is enhanced using cooper as material for the tubes. Steam cooling in combined-cycle power plants holds great promise, because turbine inlet temperature of 1649° C is possible, while metal temperature is kept below 649° C [\[3\]](#).

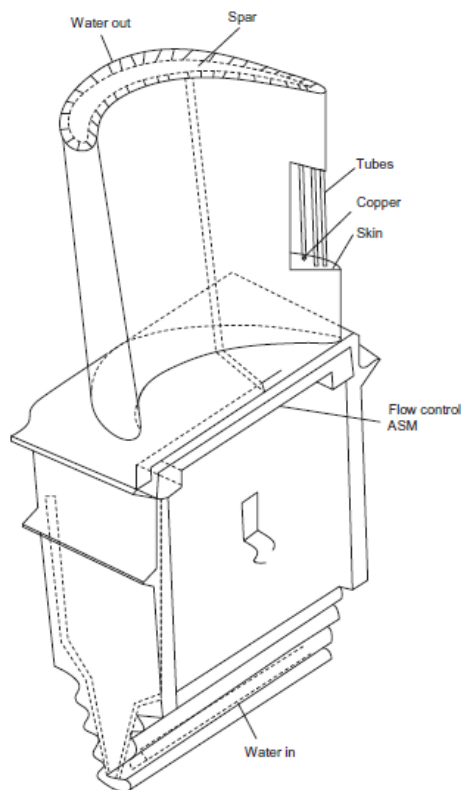


*Figure 2.12: Water-cooled turbine blade (courtesy: General Electric Company), from M.P. Boyce "Gas Turbine Engineering Handbook" (2012, pp. 415).*

### 3. *EthosEnergy Group Case: TG20B7/8 turbine*

#### 3.1 General Machine Description

TG20B7/8 is a gas turbine whose rated power is 48 MW, produced by *EthosEnergy Group* and derived from CW251B12 *Westinghouse* project. The machine is characterized by 19 compression stages; a pressure ratio of 15.4 is reached. Compressor set-up is the result of a recent redesign, carried out with commercial software for streamline flow analysis for turbomachinery. Regarding the turbine section, this is made of 3 expansion stages, which is typical for this machine size. Turbine Inlet Temperature has been increased from 788 up to 1129° C, as the project evolved throughout years. Engineers from *Ethos* decided to adopt new cooling system in 2009: this was necessary because of the tendency of clogging by fine dust particles in cooling vane insert. Reduced coolant flow in first row vane determined high deformation in many segments and, in the end, collision of statoric parts with rotating blades. Row 1 vane cooling system has been modified: according to the improved scheme, cooling air is extracted from combustor shell and directly sent to first vane of the turbine section, this avoids clogging formation for low coolant mass flow and in the end increases machine reliability. In the context of row 1 vane cooling system, also a new design of vane 1 has been considered: this has been changed from one to two-piece cooling insert. Two inserts contain multiple holes so impingement on leading edge region and film formation around the profile is present.

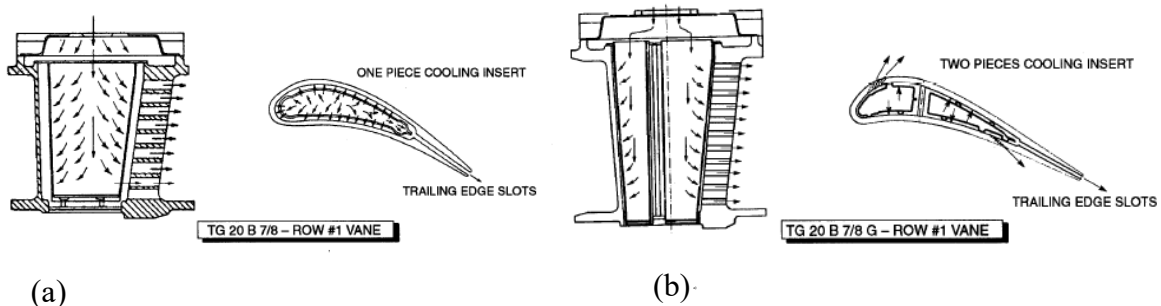


*Figure 3.1: Row 1 vane old (a) and new (b) cooling design.*

Although the TG20B7/8 is a turbine derived from old project, vane cooling design has been evolved and it's not that far from state of art vane cooling technologies adopted by segment competitors.

With improved cooling effectiveness of statoric inserts, it is worth to analyse cooling blade technology of the TG20, in order to make a comparison with refrigeration techniques described in [Chapter 2](#) and consider the degree of novelty of the adopted design.

## 3.2 Row 1 Blade Design Evolution

Under the necessity to further develop the TG20B7/8, a casting upgrade of row 1 blade is present in an internal company bulletin of 2017. In [Figure 3.2](#) is showed a 3D model of the old design of the row 1 blade of the machine. For older design, it is possible to recognize the *radial holes* cooling technology described in [2.2.1](#): heat is removed as coolant is flowing from blade's root to the tip, trough fifteen z-shaped channels. These channels are obtained from quartz rods during casting procedure. With this method, the scrap rate was huge (70%) because of component rupture during manufacturing. Any improvement has been reached also trying to change casting parameters during the procedure. Quartz rupture was mainly located in platform area: this causes holes clogging and numerous TG20/W251 Row 1 blades have been scrapped during repairing. Because of the location, mechanical method for broken quartz removal is unfeasible and the consequence is higher cost of production and, in the end, higher price per each unit sold.

For all these reasons, engineers from *EthosEnergy* decided to change manufacturing procedure: quartz rods are removed, and a ceramic core is now adopted in root region of the blade. Cooling channels are still present inside the air foil, but they're made with *Electro-Chemical Machining* (ECM) method, used for creating holes in hard materials that are difficult to machine with usual methods.

In [Figure 3.3](#) it is possible to notice difference between old blade design and new one, with ceramic core presence, instead of quartz rods.

Obviously, because of this geometric modification, thermo-mechanical response of the blade under hot gases thermal stress is expected to change: engineers from *EthosEnergy* made some predictions using many informatic tools, both commercial ones as well as Westinghouse developed software.

Thermo-structural analysis has been carried on with the following procedure:

1. Streamline analysis with *PH4187-Dynatec* software: from this analysis it was derived hot gas temperature profile along external blade surface, which is the thermal load of the system;
2. Cooling flow analysis with *PH4165* software: in this way, mass flow parameters of cooling streams inside the turbine has been obtained and it was possible to estimate heat transfer coefficient of internal cooling pipes;
3. Thermo-mechanical analysis has been carried on with *Ansys*, commercial software based on FEM numerical scheme: it was possible to obtain a precise map of temperature, tresses and strain along the entire domain, under the action of hot gases and centrifugal force;
4. Modal response analysis, in order to know response of the structure to vibration depending on its frequency.

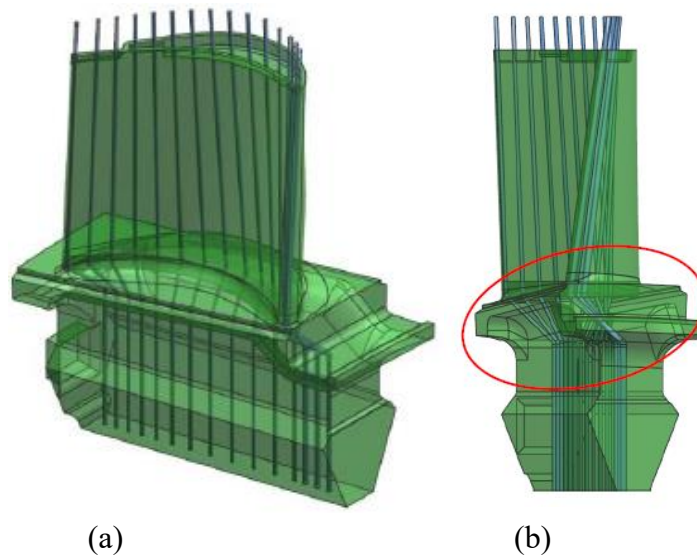


*Figure 3.2: 3D CAD model of old rotor blade of the TG20B7/8, a) with fifteen quartz rods cooling channels view and b) detail of the platform area that suffers of clogging.*

This study was made both for old and new blade design and according to these results:

- Cooling flow effectiveness is almost unchanged;
- Because of higher thermal-exchange surface in root region, maximum value of blade's temperature is slightly reduced in new design with respect to old one;
- Because of less resistant material, maximum value of stresses is slightly increased;

- Total blade deformation is reduced in new blade design;
- Modal response is unchanged from one configuration to the other.

In the end, according to simulations results, it's not possible to appreciate any change in the thermo-mechanical response of the component under external load, so design life is expected not to change from old design to new one.

But reality is different from the predicted one: TG20B7/8 turbine suffers of overheating of first rotor disc and many engines experienced an early and unexpected failure because of creep formation in rotor disc. For this reason, number of units sold in recent years is decreased.

Blade cooling plays an important role on machine failure: if an increase of refrigeration effectiveness may be possible, metal temperature distribution of the blade would decrease: blades act like fins for the rotor, so improving the cooling could also be a benefit concerning rotor disc fatigue resistance, with a possible life extension of the component.

Thus, engineers from *EthosEnergy* want to investigate more in detail thermo-mechanical behaviour of the machine and increase numerical analysis efficiency of the turbine: that's how collaboration between *EthosEnergy Group* and *Politecnico di Torino* started.

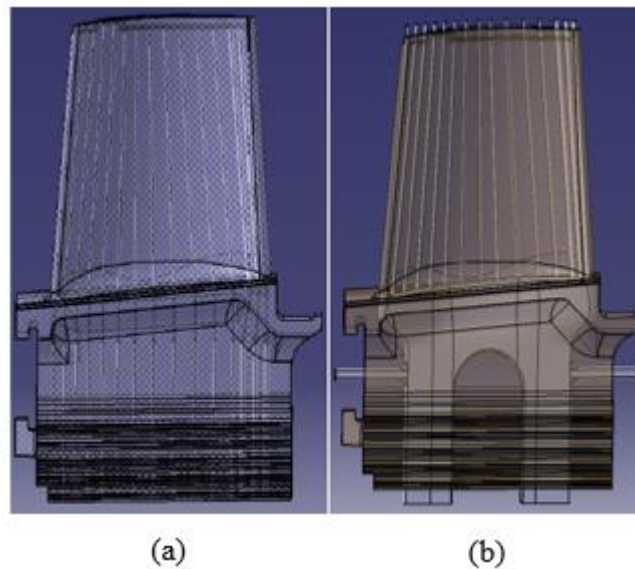


*Figure 3.3: 3D cad model of a) old and b) new cooling blade design with ceramic blade insert in place of quartz rods*

### 3.3 PH4165 Software

The program is capable of solving complex air flow networks inside *Westinghouse* project-based turbomachinery. It's used to estimate mass flow and pressure along cooling system inside the turbine. Network is modeled as a sequence of pipes (straight element with just one entry and one exit) and chambers (element in which two or more pipes converge); a flow is considered as a constant leakage to or from a chamber. For each pipe, seven different kinds of loss element may be handled:

- Pressure (P): pressure at the end of the pipe;
- Restriction (R): loss element with one velocity head loss;
- Fractional (F): loss element with a fraction of a velocity head loss;
- Seals (S): smooth labyrinth seals;
- Vortices (V): pressure change in radial direction due to solid body rotation;
- Friction (F): friction losses according to Moody diagram;
- Temperature (T): upstream temperature of the element.

Elements are then assembled in order, according to the real coolant path inside the machine: in [Figure 3.4](#) it is showed rotor cooling flow network model for old and new design of the cooling blade. Software requires as input geometry: loss elements characteristic, pressures and temperatures. Then it is asked to assume all internal chambers pressures and flow direction, and to specify tolerance for each chamber convergence. The *PH4165* software follows iterative procedure, using a “compressible adiabatic flow with losses” treatment, in order to calculate all intermediate pressures and actual flow direction. Each pipe is examined in two directions: in this way the software also handle cases for which flow direction is opposite with respect to the assumed one. For each pipe its characteristic has to be determined: in other word, the correlation between characteristic flow rate  $G \sqrt{T_{in}/T_{std}} / (p_{in}/p_{std})$  and pressure ratio between pipe inlet and outlet  $p_{in}/p_{out}$  is needed.

Starting from the analysis of loss elements upstream and downstream, the *PH4165* calculates the  $p_{in}/p_{out}$  value for no mass flow case and critic set of  $G \sqrt{T_{in}/T_{std}} / (p_{in}/p_{std})$  and  $p_{in}/p_{out}$ .

Other three sets are the  $p_{in}/p_{out}$  corresponding to 40%, 90% and 95% of critical characteristic flow rate: these sets of values have been proven to give most accurate result from curve fitting equation. With this set of five flows and pressure ratios for each flow direction, pipe

characteristic is established solving the five equations for the five unknown exponents  $a$ ,  $b$ ,  $c$ ,  $d$ , and  $e$ :

$$y_i = 10^a \sqrt{x_i} (1 + x_i)^b (1 + x_i^2)^c (1 + 5x_i^2)^d (1 + 5x_i^2)^e \quad (3.4)$$

Where  $y_i$  and  $x_i$  are proportional to  $G \sqrt{T_{in}/T_{std}} / (p_{in}/p_{std})$  and  $p_{in}/p_{out}$  respectively. Known the characteristic equation for each pipe, then it is possible to know the flow rate for any pressure ratio value in which the software may come up during the iterative procedure. Software, in the end, iterates on the chamber pressure by using the *parallel secant method*, until convergence is reached for each chamber.

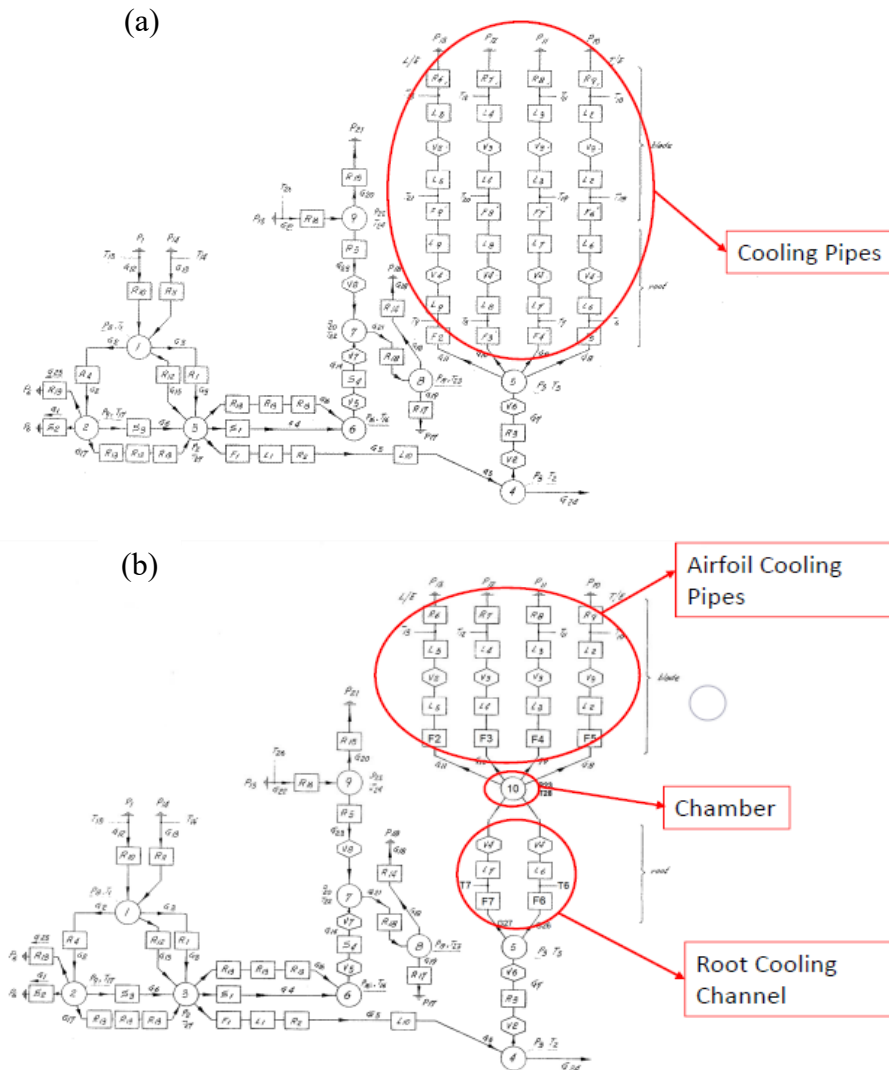


Figure 3.4: Cooling network representation for PH4165 for a) old and b) new blade cooling design.

Main software's limitation is that it is iterative procedure based, so each result is affected by a uncertainty, depending on tolerance set for each network's chamber. Another limitation is that software calculates air temperature variation along the channel, but heat balance in each chamber is not part of the main iteration, so it's neglected.

In the end, engineers from *EthosEnergy Group* complain on software's results reliability, so they wanted to investigate more in detail the cooling flow inside the *radial holes* for both old and new cooling blade design, using a more precise tool like software for Computational Fluid Dynamic analysis (CFD): main content of this study is to develop CFD analysis for cooling air path inside each row 1 rotor blade.

## 4. Theoretical Preliminaries

### 4.1 Governing Equations

General description of equations governing fluids motion is present in the following part of the thesis. Conservation equations will be presented, taking into account that fluid of interest is aeriform. If gas velocity is much less than local sound velocity, still fluid can be considered as not compressible, otherwise compressibility must be considered.

It is worth to define the *total* or *material derivative*:

$$\frac{D(\cdot)}{Dt} = \frac{\partial(\cdot)}{\partial t} + \mathbf{u} \nabla(\cdot) \quad (4.1)$$

It describes variation of a generic quantity ( $\cdot$ ) under the action of a vector field that changes along the space and it's not constant in time. As an example, the total derivative of velocity  $\mathbf{u}$  is the acceleration of fluid particle, according to Eulerian derivative rule [9].

A comprehensive derivation of following equations can be found in many books, e.g. [[Budugur Lakshminarayana, 1995](#); [Bruce R. Munson, 2010](#)].

#### Continuity equation

$$\frac{\partial \rho}{\partial t} + \nabla(\rho \mathbf{u}) = 0 \quad (4.2)$$

Where  $\rho$  denotes fluid density,  $\mathbf{u}$  the velocity vector and  $t$  is time. For compressible fluid the density represent an unknown, because is not constant and both time and space depending in the most general case.

## Momentum equations

$$\begin{aligned}\rho \frac{D\mathbf{u}}{Dt} &= \left\{ (\mathbf{u} \nabla) \mathbf{u} + \frac{\partial \mathbf{u}}{\partial t} \right\} \\ &= -\nabla p + \rho \mathbf{g} + \nabla \cdot [\mu(\nabla \mathbf{u} + (\nabla \mathbf{u})^T)] + \nabla \cdot [\lambda (\nabla \cdot \mathbf{u}) \mathbf{I}]\end{aligned}\quad (4.3)$$

First term of the equation is the total acceleration of the fluid, sum of convective (second term) and local (third term) acceleration. Fourth and fifth term are related to respectively pressure and gravitational forces, sixth and seventh term are stress tensor expression:  $\mu$  is called *shear viscosity* (or simply *viscosity*) and it measure liquid resistance of deformation by shear stresses,  $\lambda$  is called *volume viscosity* and it measure fluid resistance to volume expansion (usually neglected for incompressible fluids). This expression of the momentum equation derives from assumption of Newtonian compressible fluid; it means that strain stresses are linearly dependent to velocity gradient:

$$\tau_{ij} \propto \frac{\partial u_j}{\partial x_i} + \frac{\partial u_i}{\partial x_j} \quad (4.4)$$

Moreover, fluid is considered as isotropic. With following assumptions, equation [4.3](#) is obtained, which is one of the many possible forms of Navier-Stokes equations. Momentum must be preserved in  $x$ ,  $y$  and  $z$  direction so three equations are needed to solve the system.

## Energy equation

$$\rho \frac{Dh}{Dt} = \frac{Dp}{Dt} + \nabla \cdot (k\nabla T) + \Phi \quad (4.5)$$

Where  $h = c_p T + p/\rho$  is the specific enthalpy,  $T$  is temperature and  $k$  is thermal conductivity of the fluid.

First term of equation [4.5](#) is total rate of change (both local and convective) of enthalpy,  $Dp/Dt$  is rate of work done by pressure, third term is conductive heat exchange inside the fluid.

The last term in right-hand side ( $\Phi$ ) is equivalent mechanical rate of work due to viscous dissipation:

$$\Phi = \mu \left[ 2 \left( \frac{\partial u}{\partial x} \right)^2 + 2 \left( \frac{\partial v}{\partial y} \right)^2 + 2 \left( \frac{\partial w}{\partial z} \right)^2 + \left( \frac{\partial v}{\partial x} + \frac{\partial u}{\partial y} \right)^2 + \left( \frac{\partial v}{\partial z} + \frac{\partial w}{\partial y} \right)^2 + \left( \frac{\partial u}{\partial z} + \frac{\partial w}{\partial x} \right)^2 \right] + \lambda (\nabla \mathbf{u})^2 \quad (4.6)$$

For incompressible fluids, energy equation can be solved after continuity and momentum equation are solved, and temperature profile inside the fluid is calculated.

For compressible fluids, still density is unknown, so we need fourth equation in order to couple pressure and density.

### Equation of state

$$p = \rho RT \quad (4.7)$$

Where  $R$  is the specific constant of the gas. At air conditions of our interest, ideal gas approximation can be reasonably made.

With this set of 6 equations we can calculate all the sixth unknowns: three velocity components ( $\mathbf{u}$ ), pressure ( $p$ ), temperature ( $T$ ) and density ( $\rho$ ).

This system completely describes compressible fluid motion: exact solution can be calculated only for very special problems and, in most of the cases, numerical methods must be used in order to have physics behind the phenomenon.

## 4.2 Finite Volume Method

Finite Volume Method is the numerical scheme adopted in most of commercial CFD software. This method was developed at the end of the fifties: its main advantage is that, although variables may not be continuous due to shock or boundary discontinuity, momentum and energy are always preserved. Another advantage is that cell shape is not limiting the conservative property of the numerical method, so meshing can be accomplished with many possible cell's shape. Drawback is that false diffusion may be present if poor numeric is used.

The Finite Volume Method is based on integral form of conservation equation of a generic quantity  $\phi$  in steady state condition:

$$\int_S \rho \phi \mathbf{u} \cdot \mathbf{n} dS = \int_S \Gamma \nabla \phi \cdot \mathbf{n} dS + \int_{\Omega} q_{\phi} d\Omega \quad (4.8)$$

Where  $\Gamma$  is the diffusive coefficient of  $\phi$  and  $q_{\phi}$  is a volumetric source term. Equation 4.8 stands that surface integral of convective flux component ( $\rho \phi \mathbf{u}$ ) is equal to surface integral of diffusive flux component ( $\Gamma \nabla \phi$ ) plus volume integral of the volumetric source term ( $q_{\phi}$ ).

This conservation equation is applied for each control volume in which domain is sub-divided: an example is showed in figure below [10].

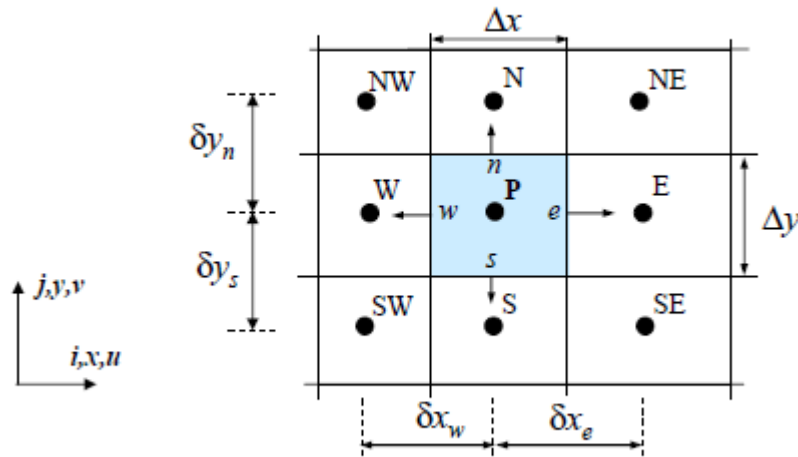


Figure 4.1: Example of Finite Volume grid (source: Andre Bakker CFD course)

Each cell has a node (capital letter), where quantities of interest are evaluated. For a 2D case, each Control Volume has four boundary surfaces (lowercase letters), in which surface integrals have to be estimated. Dimension of the cell is  $\Delta V = \Delta x \cdot \Delta y$ .

It is possible to use this cartesian grid example in order to develop passages for equation 4.8 discretization, which is an approximated algebraic form suitable for the computer calculation. Numerical approximation for both surface and volume integral of conservative equation is needed; moreover, we need to approximate  $\phi$  value at each boundary in terms of nodal values. These will be the contents of the next section, as well as an overview of Navier-Stokes non-linearity treatment.

### 4.2.1 Integrals Approximation

According to conservative equation, flux of a generic function  $f$  through CV boundary has to be considered. This can be decomposed as:

$$\int_S f dS = \sum_k \int_{S_k} f dS \quad (4.9)$$

The net flux through CV boundary is the summation of integrals of  $k^{th}$  surface, with  $k=1, \dots, 4$ . In order to properly develop these integrals, one would properly know values of integrand  $f$  everywhere on the surface  $S_k$ . We need to approximate integral value at one or more locations on cell face. This can be accomplished with *midpoint rule*: Integral is approximated as product of integrand value at cell-face centre (which is approximated as mean value over the surface) and the cell-face area:

$$F_e = \int_{S_e} f dS = \bar{f}_e S_e \approx f_e S_e \quad (4.10)$$

Where  $F_e$  is the integral value at east boundary,  $f_e$  is the integrand value at east cell face centre and  $S_e$  is east-boundary area. As already said,  $f_e$  value is not available so it must be obtained by interpolation from nodal values of the integrand. There are other possible formula for integral approximation, like *trapezoidal rule* or *Simpson's rule*; reference is made to other texts [\[11\]](#).

Approximation increases its validity as boundary surface gets smaller; in other words, error related to the integral approximation is reduced as surface of interest decreases. In particular, midpoint rule is second order accuracy: it means that two order of magnitude error reduction is obtained as a result of one order of magnitude grid refinement.

Regarding the source term in transport equation, it requires integration over the entire volume of the cell. Simplest way is to replace volume integral as product between integrand at cell centre and CV volume:

$$Q_P = \int_{\Omega} q d\Omega = \bar{q} \Delta\Omega \approx q_p \Delta\Omega \quad (4.11)$$

Where  $q_p$  is the volumetric source term at CV center. No interpolation is needed because source term is known at node P. Previous approximation becomes exact if  $q$  is either constant or varies linearly within the CV; otherwise, it is of second-order accuracy [11].

#### 4.2.2 Interpolation

To calculate convective and diffusive flux on each cell boundary, value of  $\phi$  as well as its derivative is needed. Due to lack of this information, it's needed to have approximated value of  $\phi_e$  referring to nodal value  $\phi_P$ . Numerous possibilities are available so a few of them are mentioned.

#### Upwind Differencing Scheme (UDS)

It's equivalent to a forward or backward-difference approximation, depending on “wind” direction:

$$\phi_e = \begin{cases} \phi_P & \text{if } (\mathbf{u} \cdot \mathbf{n})_e > 0 \\ \phi_E & \text{if } (\mathbf{u} \cdot \mathbf{n})_e < 0 \end{cases} \quad (4.12)$$

This is a first-order scheme so second order accuracy from midpoint rule is lost. On the other hand, it's a very stable method and it will never yield to oscillation. However, this is achieved by being numerically diffusive: it means that effective diffusivity will be given by:

$$\Gamma_{eff} = \Gamma + \frac{(\rho \mathbf{u})_e \Delta x}{2} \quad (4.13)$$

A numerical diffusivity  $\Gamma_{num} = (\rho \mathbf{u} \cdot \mathbf{n})_e \Delta x / 2$  is introduced, which is magnified in multidimensional problems if the flow is oblique to the grid: it determines to have extra diffusion in flow direction as well as streamwise direction. It is also hard to reduce  $\Gamma_{eff}$  because it derives from truncation error and because upwind scheme is only first order accurate, great mesh refinement is needed in order to appreciate any reduction of numerical diffusivity.

## Central Difference Scheme (CDS)

Another possible approximation is linear one between the two nearest nodes:

$$\phi_e = \phi_E \lambda_e + \phi_P (1 - \lambda_e) \quad (4.14)$$

Where linear interpolation factor  $\lambda_e$  is defined as:

$$\lambda_e = \frac{x_e - x_P}{x_E - x_P} \quad (4.15)$$

Leading truncation error is of the second order, therefore is more accurate with respect to UDS. Main issue of this numerical scheme is that it's lacking of *transportiveness* property: it's not able to recognize flow direction which affects convection term. This may cause oscillation depending on *Peclet mesh number*:

$$Pe = \frac{\rho u \Delta x}{\Gamma} \quad (4.16)$$

If  $Pe > 2$ , then numerical oscillation is present. One could use CDS if  $Pe < 2$ , otherwise UDS must used: such approach is called *hybrid scheme*.

## Second Order Upwind Scheme

It's an evolution of UDS:  $\phi_e$  value is calculated considering a linear interpolation of two nodal values upstream the face. It's harder to implement but, in this way, it is possible to reach second order accuracy; moreover, numerical diffusion can also be reduced taking advantage of higher order of accuracy. Second Order Upwind Scheme is one of the most popular numerical models, because of its combination of stability and precision.

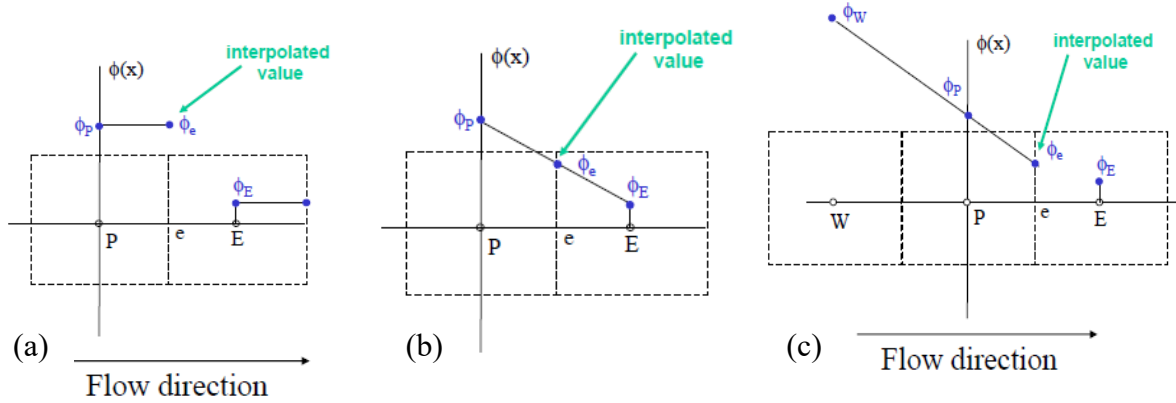


Figure 4.2: Representations of a) UDS, b) CDS and c) second order UDS (source: Andre Bakker CFD course)

### 4.2.3 Iterative Procedure

Conservation equation 4.8 can be solved only if density and velocity field is known, otherwise we need to refer to equations described in 4.1: it can be noticed that it's not possible to write a conservation equation for pressure, and it has to be derived from momentum equation. This condition is known as *pressure-velocity coupling* and impose that the solution of the system can be accomplished only by iterative procedure. Algorithms are needed in order to derive pressure value from continuity and momentum equation: most used one is called SIMPLE (Semi-Implicit Method for Pressure Linked Equations) in which at each iteration pressure imbalance is calculated according to:

$$a_p p' = \sum_{nb} a_{nb} p' + b' \quad (4.17)$$

Where  $b'$  is the mass flow imbalance and  $a$  coefficients depend on grid size and velocity field. At successive iteration, pressure is corrected with pressure imbalance.

SIMPLE algorithm is based on the fact that fluid flows from high pressure to low pressure regions: if mass flow imbalance denotes more flow into the cell with respect to surrounding cells, then pressure value have to be increased; opposite operation is made if mass flow value in the specific cell is higher with respect to surrounding cells.

Because of the iterative nature of the solver, at each node P a new value of the generic quantity  $\phi_P$  is calculated; this is subjected to a certain relaxation:

$$\phi_p^{new,used} = U (\phi_p^{new,predicted} - \phi_p^{old}) \quad (4.18)$$

Where  $U$  is the *relaxation factor* that can be:

- $U < 1$  is *under-relaxation*: it slows down simulation convergence but increase stability of the solution, avoiding dumping;
- $U = 1$  is *no relaxation*: predicted solution is not treated;
- $U > 1$  is *over-relaxation*: it can be used to accelerate convergence but decrease simulation's stability.

Relaxation factor has to be kept low for difficult physics problem during initial iterations, then it can also be increased for solution acceleration.

Convergence is reached if all quantities computed are basically not changing from one iteration to the successive. One possible convergence indicator is *residual*, which is difference in absolute value between right-hand side and left-hand side of conservative equation: a simulation is converging if, as iterations proceeds, residuals decreases. Each simulation is characterized by a certain number of residuals, depending on the number of equations solved at each iteration. It can't be said that convergence is reached if residuals are stable; as a matter of fact, it is mandatory to verify stability of a physical monitor before concluding that solution has converged: this situation was very common during the simulations that will be presented in the next chapters.

#### 4.2.4 Finite Volume Solution Implementation

Solution of the set of equation seen in [4.1](#) can be accomplished in many ways, depending on the algorithm adopted by the computational solver. As a matter of fact, for a steady state problem, we may decide to solve first continuity and momentum equation (according to pressure-velocity coupling algorithm) at each iteration and then solve other equations like energy equation and turbulence model equations: this approach is called *segregated solution procedure*. This solver is usually the one pre-set in most of the commercial software because

it's less CPU demanding, so it's easier to implement. It is good practice do adopt a segregated solver only in case of incompressible flows, or compressible flows at low Mach number ( $Ma < 0.3$ ): this because density is known for this kind of problems, so continuity and momentum equations can be solved independently.

In the case that the problem of interest involves compressible flows, especially with shock wave, it's better to adopt a *coupled solution procedure*: continuity, momentum and energy equation are solved all together; then equations involving other scalars (like turbulence related ones) are solved. When coupled solver is involved in a steady state calculation, it essentially employs a modified version of a transient calculation, with a fictitious time step depending on:

$$\Delta t = \frac{CFL \cdot x}{u} \quad (4.19)$$

Where  $x$  is characteristic length of the cell,  $u$  is local velocity measure and  $CFL$  is the *Courant-Friedrich-Levy number*, a parameter set by the user. Increasing CFL number, pseudo time-step increases so solution can be speeded up but also oscillation may arise.

In the following chapters also results of some transient simulations will be presented. In many cases, for some difficult physics, it's better to adopt an unsteady solution procedure, even if transient behaviour it's not of interest. In this case, both segregated or coupled approach can be used; time-step is set by the user and a certain number of iterations per time-step are made: when convergence is reached, the software updates the solution and proceeds the calculation advancing in time. If an accurate transient solution is needed, convergence should be reached for each time-step, otherwise it may not be necessary.

### 4.3 Turbulence Modelling

Turbulence is always present in our life: from sugar dissolving in a coffee thanks to spoon action, to rocket taking off for a space mission; when a fluid motion acts in unstable and chaotic way, we talk about turbulent regime. This behaviour appears when Reynolds number overtake a certain limit, which is characteristic of the specific case. This flow regime is totally the opposite of laminar flow, in which particle motion is easily predictable thanks to fluid dynamic equations. Turbulence result from the fact that, at high Reynolds number, flow inertia overcome

viscous stresses and laminar motion becomes in the end unstable. Due to turbulence, all the physical quantities describing dynamic of the fluid are affected by fluctuation, so they are both changing in space and time. Thus, turbulent flow is always three-dimensional and time depending: an enormous quantity of information is needed to its complete description. The more is the level of detail needed, the more complicated will be the mathematical method required: rule of the engineer is to adopt in a conscious way the conceptually simplest numerical model available, in order to achieve his goal.

#### 4.3.1 Kolmogorov Theory

Due to its chaotic behaviour, turbulent flow can't be described in a deterministic way but just probabilistic. When describing turbulence, many researchers refer to eddying motion, which is local swirling: this mean that turbulent fluid is always with non-zero vorticity. Moreover, eddies are present in wide range of size, bigger ones usually transfer kinetic energy to the smaller ones, with a process that is always dissipative because kinetic is converted into heat. Turbulence provides great mixing and increases diffusion of energy, mass and momentum.

Another important property is that turbulence is a continuous phenomenon: even if eddies scale range is wide, minimum eddy dimension is always much larger than the molecular scale. This was proved by Kolmogorov: according to his theory, defining  $k$  the *turbulence kinetic energy*, smallest scale eddies depend on just rate at which larger eddies provides kinetic energy  $\epsilon = -dk/dt$ , and kinematic viscosity  $\nu$ . With just a dimensional analysis, starting from these two quantities, Kolmogorov derived following length ( $\eta$ ), time ( $\tau$ ) and velocity ( $v$ ) scale:

$$\eta = (\nu^3 \epsilon)^{1/2}; \quad \tau = (\nu \epsilon)^{1/2}; \quad v = (\nu \epsilon)^{1/4} \quad (4.20)$$

These are *Kolmogorov scale* of length, time and velocity. Proceeding on his studies, the mathematician developed a spectral distribution analysis, due to the fact that turbulence involves a continuous spectrum of scale. Kinetic energy ( $k$ ) is decomposed in *wavenumbers*  $\kappa$  or in wavelength  $\lambda = 2\pi/\kappa$ .

It can be demonstrated that  $\kappa$  is the reciprocal of eddy size [\[12\]](#).

Defining  $E(\kappa)$  the turbulent kinetic energy per unit of mass between wavenumbers  $\kappa$  and  $\kappa + d\kappa$ , then total kinetic energy per unit of mass is given by:

$$k = \int_{-\infty}^{+\infty} E(\kappa) d\kappa \quad (4.21)$$

Thus, *energy spectral density*  $E(\kappa)$  is related to the Fourier transform of  $k$ .

Total kinetic energy is mainly depending on largest eddies, which length scale is denoted as  $l$  and it's called *integral length scale*. If it is assumed that  $l \gg \eta$ , then it exists a wide range of scale from largest eddies to Kolmogorov's scale eddies: in the middle exists a range of wavenumber, in which energy transfer is dominated by inertial effects. This brought Kolmogorov to conclude that:

$$E(\kappa) = C_k \epsilon^{2/3} \kappa^{-5/3}; \quad \frac{1}{l} \ll \kappa \ll \frac{1}{\eta} \quad (4.22)$$

Where  $C_k$  is the *Kolmogorov's constant* and the previous equations is called *-5/3 rule*. The existence of the so called *Inertial Sub-Range* has been proved in many practical experiences: an example of real energy spectral density is showed in following double logarithmic plot, where the inertial sub-range is highlighted.

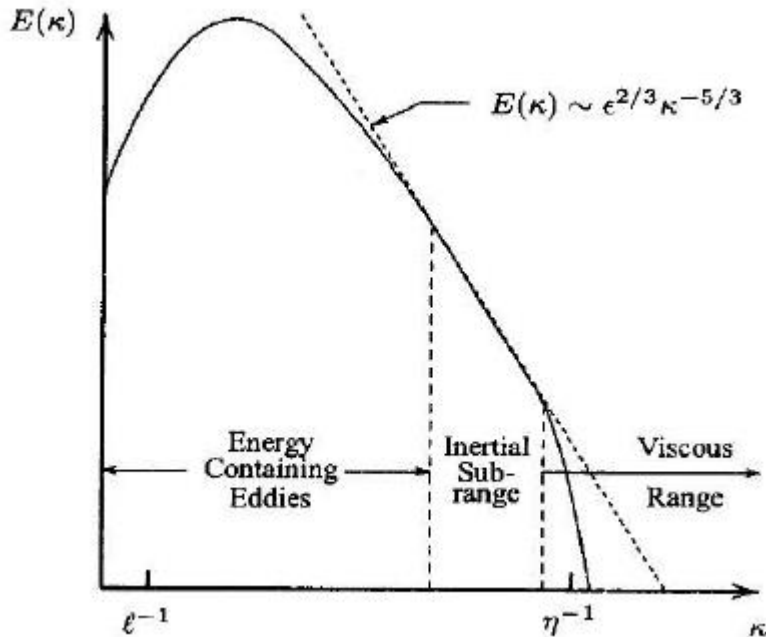


*Figure 4.3: Energy Spectrum for a Turbulent flow in log-log scale (source: D.C. Wilcox, "Turbulence Modelling for CFD"; DWC Industries, 2006, p.p. 13).*

A numerical turbulence model that is not presenting the  $-5/3$  rule in inertial sub-range can't be considered as acceptable.

According to energy spectrum for a turbulent flow, for low wavenumbers  $\kappa$ , size of the eddies is larger so characteristic length is closer to the integral length scale  $l$ : this range is related to the *Energy Containing Eddies*, due to their larger size. For higher wavenumbers  $\kappa$ , size of the eddies is reducing up to Kolmogorov length scale  $\eta$ ; this region of the energy spectrum is called *Viscous Range* because size of the eddies is so small that viscous forces exceed inertial ones.

#### 4.3.2 Reynolds-Averaged Navier-Stokes Equations

According to the energy spectrum of [Figure 4.3](#), turbulent flow contains a wide range of length and time scales, so complexity of the approach will depend on level of detail of interest. Most detailed procedure is the so called *Direct Numerical Simulation* (DNS), in which Navier-Stokes equations are completely solved and eddies behaviour is fully described; from largest one up to the Kolmogorov length scale, the simulation carries on a transient study that reaches a level of detail according to the time scale  $\tau$ . This approach is the simplest one from the conceptual point of view but it represent a huge expenditure in term of computational effort: it has been showed that, for isotropic turbulence, a complete description of the phenomenon requires at least a number of grid points in each direction that is proportional to  $Re^3$ ; with  $Re$  of the order of magnitude of  $\sim 5000$  for typical turbulent flows: this mean a grid size of about  $10^{11}$  nodes. This huge quantity of information isn't necessary in many cases; moreover, this method is too expensive and can't be used as a design tool.

Another approach would be to consider just large-scale motion, which is carrying most of the energy involved in turbulent phenomenon: analysis that are based on this assumption are called *Large Eddy Simulations* (LES). This method is the preferred one either when Reynold number is too big or geometry too complex for application of DNS. If LES is adopted, behaviour of bigger eddies is still fully evaluated but the ones in the viscous range are just modelized. Still computational effort remains very large and, for an engineering point of view, this quantity of extrapolated information may be not necessary; usually an average information is simply needed.

Based on a Reynolds' intuition, every physical quantity that varies due to turbulence action can be decomposed as summation of a time averaged value and a fluctuation about that value:

$$\phi(x_i, t) = \bar{\phi}(x_i) + \phi'(x_i, t) \quad (4.23)$$

Where the time-averaged value of  $\phi$  in steady state condition is defined as:

$$\bar{\phi}(x_i) = \lim_{T \rightarrow \infty} \frac{1}{T} \int_0^T \phi(x_i, t) dt \quad (4.24)$$

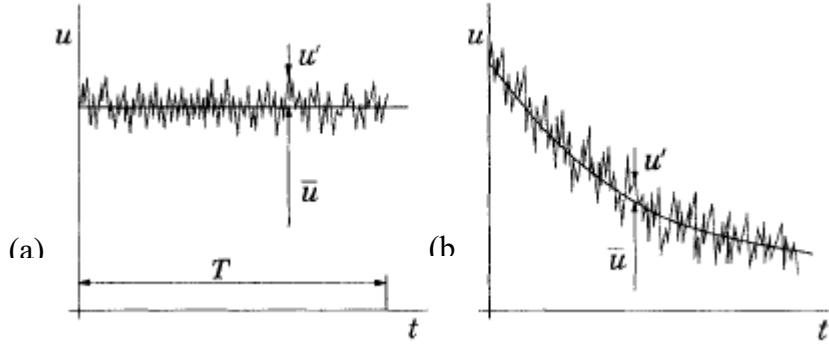


**Figure 4.4:** Time averaging for a) statistically steady flow and b) ensemble averaging for unsteady flow (source: J.H. Ferziger, M. Peric, “Computational Methods for Fluid Dynamics”; Springer-Verlag, 2002, p.p. 293).

As is showed in [Figure 4.4](#), also average quantity  $\bar{\phi}$  may be time dependent; in that case, time averaging is replaced by ensemble averaging:

$$\bar{\phi}(x_i) = \lim_{N \rightarrow \infty} \frac{1}{N} \sum_{n=1}^{\infty} \phi(x_i, t) \quad (4.25)$$

Models derived from *Reynolds-Averaged Navier-Stokes (RANS) equations* are based on the assumption that turbulence flow can be analysed just under average prospective. When averaging conservation equations, all the linear terms in the equations becomes the identical terms but averaged; this is because  $\overline{\phi'} = 0$ .

Result of averaging procedure for a quadratic non-linear term is the product of the average quantities plus covariance term:

$$\overline{u_i \phi} = \overline{(\bar{u}_i + u'_i)(\bar{\phi} + \phi')} = \bar{u}_i \bar{\phi} + \overline{u'_i \phi'} \quad (4.26)$$

Time averaged continuity, momentum and scalar quantity conservation equation for an incompressible flow are presented below:

$$\frac{\partial(\rho\bar{u}_i)}{\partial x_i} = 0 \quad (4.27)$$

$$\frac{\partial(\rho\bar{u}_i)}{\partial t} + \frac{\partial}{\partial x_j}(\rho\bar{u}_i\bar{u}_j + \rho\overline{u'_i u'_j}) = -\frac{\partial\bar{p}}{\partial x_i} + \frac{\partial\bar{\tau}_{ij}}{\partial x_j} \quad (4.28)$$

$$\frac{\partial(\rho\bar{\phi})}{\partial t} + \frac{\partial}{\partial x_i}(\rho\bar{u}_i\bar{\phi} + \rho\overline{u'_i\phi'}) = \frac{\partial}{\partial x_i}\left(\Gamma\frac{\partial\bar{\phi}}{\partial x_i}\right) \quad (4.29)$$

Where  $\bar{\tau}_{ij}$  is the mean viscous stress tensor:

$$\bar{\tau}_{ij} = \mu\left(\frac{\partial\bar{u}_i}{\partial x_j} + \frac{\partial\bar{u}_j}{\partial x_i}\right) \quad (4.30)$$

We can notice that, applying time average operator at conservation equations, still fluctuating terms survives; these are  $\overline{\rho u'_i u'_j}$ , which is called *Reynolds stresses*, and  $\overline{\rho u'_i \phi'}$ , which is called *turbulent scalar flux*.

Although some fluctuating terms are still present, a huge simplification has been obtained: turbulence modelling becomes just a matter of *closure problem*, which means to find correlations for describing in a proper way the Reynold stresses and the turbulent scalar flux.

A great variety of turbulence models based on RANS exists: each of them has its pros and cons and some are more indicated for certain problems instead of others.

Following section will be devoted on a brief presentation of the turbulence model adopted during all the simulations that are part of the present work.

### 4.3.3 *k-ε Model*

This two-equation model is the most widely adopted and validated turbulence model; its typical application ranges from industrial related to natural convection flows. On the other hand, it has been proved that k-ε model is less reliable in problems that involve reverse pressure gradient, very curved boundary layers, rotating flows or non-circular ducts.

The model is based on *Boussinesq approximation*, or *eddy-viscosity model* for the Reynold stresses:

$$-\rho \overline{u'_i u'_j} = \mu_t \left( \frac{\partial \bar{u}_i}{\partial x_j} + \frac{\partial \bar{u}_j}{\partial x_i} \right) \quad (4.31)$$

As time average shear stresses are related to molecular viscosity, in a similar way Reynolds stresses can be reasonably related to mean shear stresses considering the *turbulent viscosity*  $\mu_t$ : this is reasonable because turbulence determines increase of momentum dissipation.

With the same argument, also diffusion of scalar quantity  $\phi$  is increased thanks to turbulence; this leads to *eddy-diffusion model*:

$$-\rho \overline{u'_i \phi'} = \Gamma_t \frac{\partial \bar{\phi}}{\partial x_i} \quad (4.32)$$

*Turbulent diffusivity*  $\Gamma_t$  is related to turbulent viscosity:

$$\sigma_t = \frac{\mu_t}{\Gamma_t} \quad (4.33)$$

Where  $\sigma_t$  is called *turbulent Schimdt number*, which it has been proved to be constant, with values in the ranges between 0.7 and 1 [10].

Thus, turbulence modelling is just a matter of finding proper value of  $\mu_t$ ; in this approach, turbulent viscosity is assumed as a constant, but this approximation may not be valid in many cases and in more complex models  $\mu_t$  is a tensor.

In this model, the eddy viscosity is expressed as:

$$\mu_t = \rho C_\mu \frac{k^2}{\varepsilon} \quad (4.34)$$

It's a function of turbulent kinetic energy  $k = 1/2 (\overline{u'_x u'_x} + \overline{u'_y u'_y} + \overline{u'_z u'_z})$  and turbulent dissipation rate  $\varepsilon$ . Parameter  $C_\mu$  is usually equal to 0.09. Other two conservative equations are

needed, for both  $k$  and  $\varepsilon$  quantity: for details of the derivations of these, as well as parameters values that are present, see book by Wilcox [\[12\]](#).

We conclude saying that, although there is little difficulty on discretization of these equations, due to the fact that time scale in which turbulent phenomenon takes place is much shorter than those connected with mean flow,  $k$  and  $\varepsilon$  conservation equations are much stiffer so they need special treatment for their proper solution.

Hence,  $k$  and  $\varepsilon$  equations are not solved coupled with the other equations and, according to iterative procedure seen in [4.2.4](#), first pressure-velocity in the inner iterative loop is solved, using  $\mu_t$  of the previous iteration; then  $k$  and  $\varepsilon$  equations are solved, with new  $\mu_t$  calculated from external iterations. Another effect of the too large time step is that  $k$  and  $\varepsilon$  values are greatly oscillating and they even may come up to negative values: that's why relaxation procedure as seen in [4.2.3](#) is needed for these terms.

## 5. First Case Study: Radial Holes Cooling Channels

First part of this study is devoted on numerical analysis of the old cooling system adopted in row 1 vane blade of the TG20B7/8 turbo gas machine. Main content of this chapter is a report of how simulations have been implemented and all the results from the analysis. In the end, aim of this study was to have a validation of *PH4165* software results, so always a comparison of results coming from two software is present. We started from the analysis of a single channel, in order to find proper meshing procedure on a limited portion of the domain; then analysis was extended to a three channels group, all with the same boundary conditions and then, result from complete geometry simulation will be presented.

### 5.1 One Channel Geometry: Grid Independence Study

CFD analysis started from simulation of just one channel of the cooling system; taking advantage of a simple geometry, we were able to try many different meshing procedures and to develop a sensitive analysis in order to find proper number of cells for domain discretization. Grid independence study means that a series of analysis has been made, changing number of the cells in the domain and looking how monitors values changes and making some considerations about error connected to discretization. Aim of the grid independence study is to characterize each mesh with a certain error with respect to solution with larger number of cells and in the end choice mesh size that is good compromise between accuracy of the results and computational cost.

First, geometry of the system is presented in [Figure 5.1](#): domain is composed by the third channel of the blade with respect to leading edge; two fictitious chambers has been introduced at the inlet and outlet of the system. Function of each plenum is to impose in a proper way pressure at inlet and outlet of the channel. According to data from *EthosEnergy Group*, it is known absolute total pressure both at inlet and outlet of each of the fifteen channels of the domain but, in order to properly impose this condition, in both inlet and outlet surface of the two chambers a stagnation condition is imposed. In the case of channel #3 we have that static absolute pressure is  $p_{in} = 9.55 \text{ bar}$  and outlet pressure is  $p_{out} = 6.38 \text{ bar}$  Thus, for a given pressure drop along

the channel, consequent mass flow is compared with the one computed by *PH4165* software. Cooling air is heated by the action of the hot gases from the combustor, through a conjugated heat transfer phenomenon that involves metal surface of the blade: company's software is also giving an estimation of air temperature at the inlet and outlet of the channel. In order to validate also these data, inlet temperature boundary condition was imposed equal to *PH4165* ( $T_{in} = 659.89 \text{ K}$ ) and heat flux on each channel, according to input data, was calculated as  $Q \doteq \dot{m} \bar{c}_p (T_{out} - T_{in})$  and imposed at channel's wall: so temperature at the outlet of the channel is considered a monitor in order to validate *PH4165* software results. Grid independence study has been carried on with  $Q = 0.419 \text{ kW}$  then in final results section, all the data are results of a simulation with  $Q = 0.824 \text{ kW}$  and  $T_{in} = 529.44 \text{ K}$ , in order to appreciate system response to different heat loads.

All the simulations are based on a coupled approach in steady state condition: this choice was made because, from past works emerged that air reaches high Mach number at channel's outlet, so flow can't be considered as incompressible; thus, this solver is more advisable. Turbulence model adopted is k- $\epsilon$  due to its strong reliability as well as lack of possible detachment region in the domain as well as not expected reverse pressure.

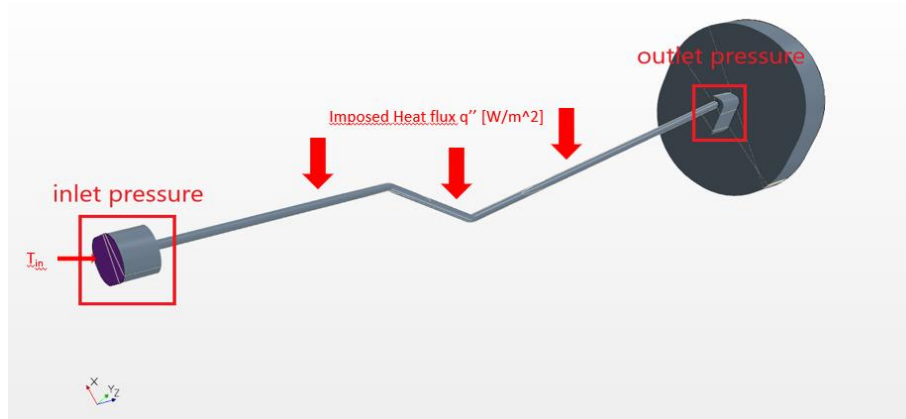


*Figure 5.1: Geometry of the system and representation of boundary conditions imposed.*

### 5.1.1 Prism Layers Sensitive Analysis

Grid independence study started from the analysis of the number of prism layers: these are particular cells located close to the boundary of the domain where special physical conditions are present. During all the simulations, boundary layer problem has been approached using an

*all y+ treatment*: if cell is too big in comparison to velocity field at the boundary, flow interaction with channel's wall is not computed but modelled using a wall function. If this method is used in a simulation, first of all, proper number of prism layers have to be determined. All the simulations have been carried on using a polyhedral cell geometry: different meshing approach has been considered for channel region and control volumes region at inlet and outlet: base size of channel's cells is 0.64 mm, while for control volume regions, the fixed base size is 0.8 mm and number of prism layers is just one, due to lack of interest of flow inside this subset of the domain: as a matter of fact, they're just necessary in order to properly impose inlet and outlet pressure boundary conditions. Maximum number of 20'000 iterations has been set as stopping criteria: convergence has been reached for all the simulations. Monitors used in order to carry on this analysis were: mass flow calculated at inlet and outlet of the channel, absolute total pressure at inlet and outlet, pressure drop along the channel and bulk temperature at the outlet. Results of this analysis are reported in [Table 5.1](#).

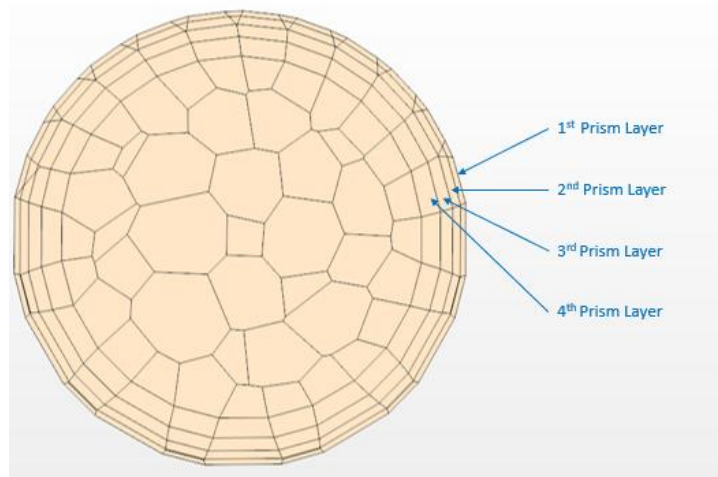


**Figure 5.2:** Polyhedral mesh in channels region (cross section), base size of 0.64 mm, 4 prism layers detail.

Prism Layers	Cells	$\dot{m}_{in}$ [g/s]	$\dot{m}_{out}$ [g/s]	$\Delta\dot{m}$ [%]	$p_{in}$ [bar]	$p_{out}$ [bar]	$\Delta p$ [bar]	$T_{bulk}$ [K]
1	55439	3.576	3.594	0.497	9.01	7.59	1.41	763.36
2	69326	3.440	3.452	0.370	8.89	7.50	1.39	766.93
3	83213	3.415	3.426	0.319	8.87	7.47	1.40	767.51
4	97159	3.414	3.439	0.732	8.89	7.50	1.39	767.48
5	111046	3.391	3.415	0.692	8.90	7.48	1.41	768.30

**Table 5.1:** Results from sensitive analysis on number of prism layers

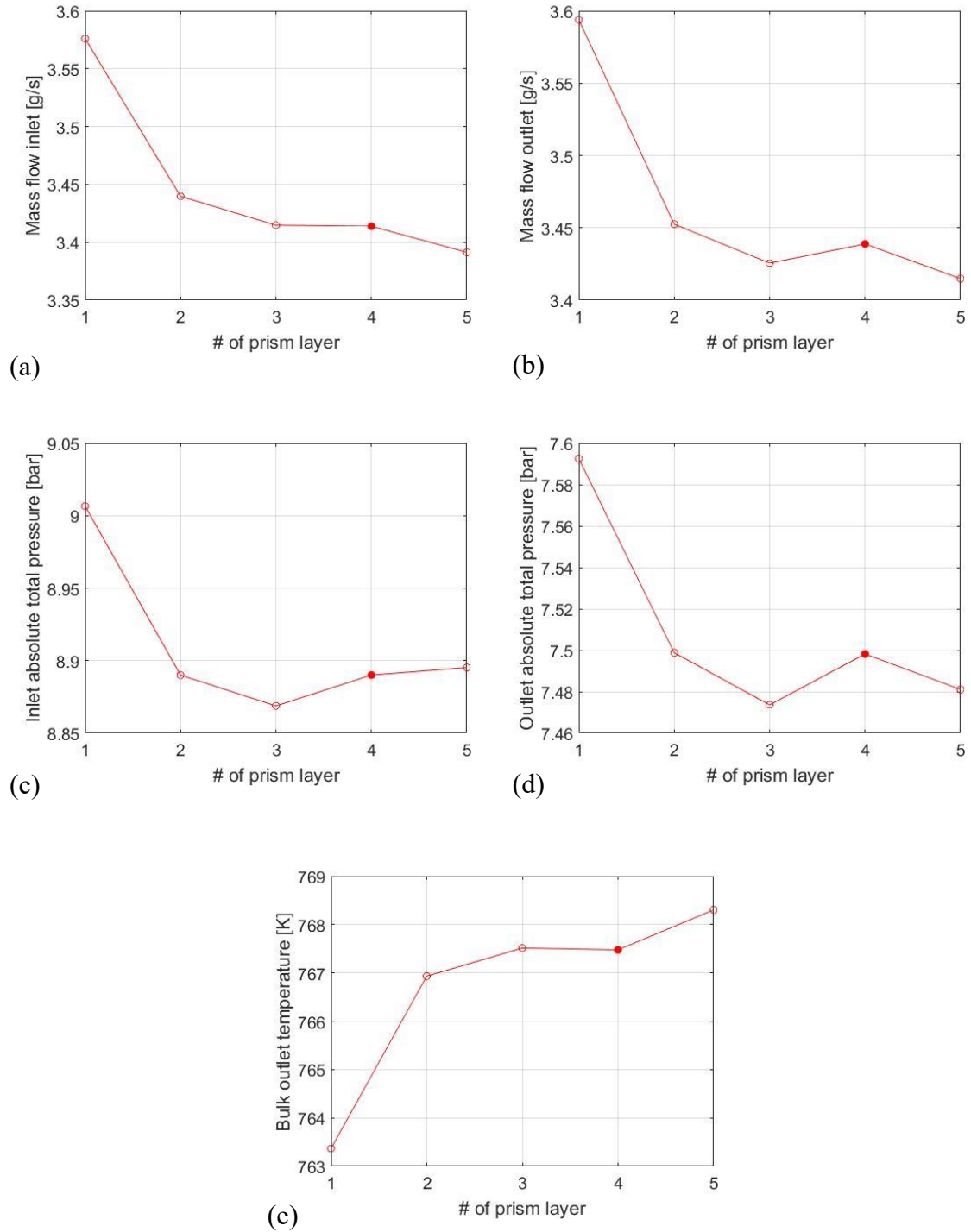


**Figure 5.3:** Computed quantities for each monitor and their extrapolated value, for many prism layers values of simulations with polyhedral mesh; a) inlet mass flow, b) outlet mass flow, c) inlet absolute total pressure, d) outlet absolute total pressure, e) outlet bulk temperature; Marked value is the monitor value for the adopted number of prism layers.

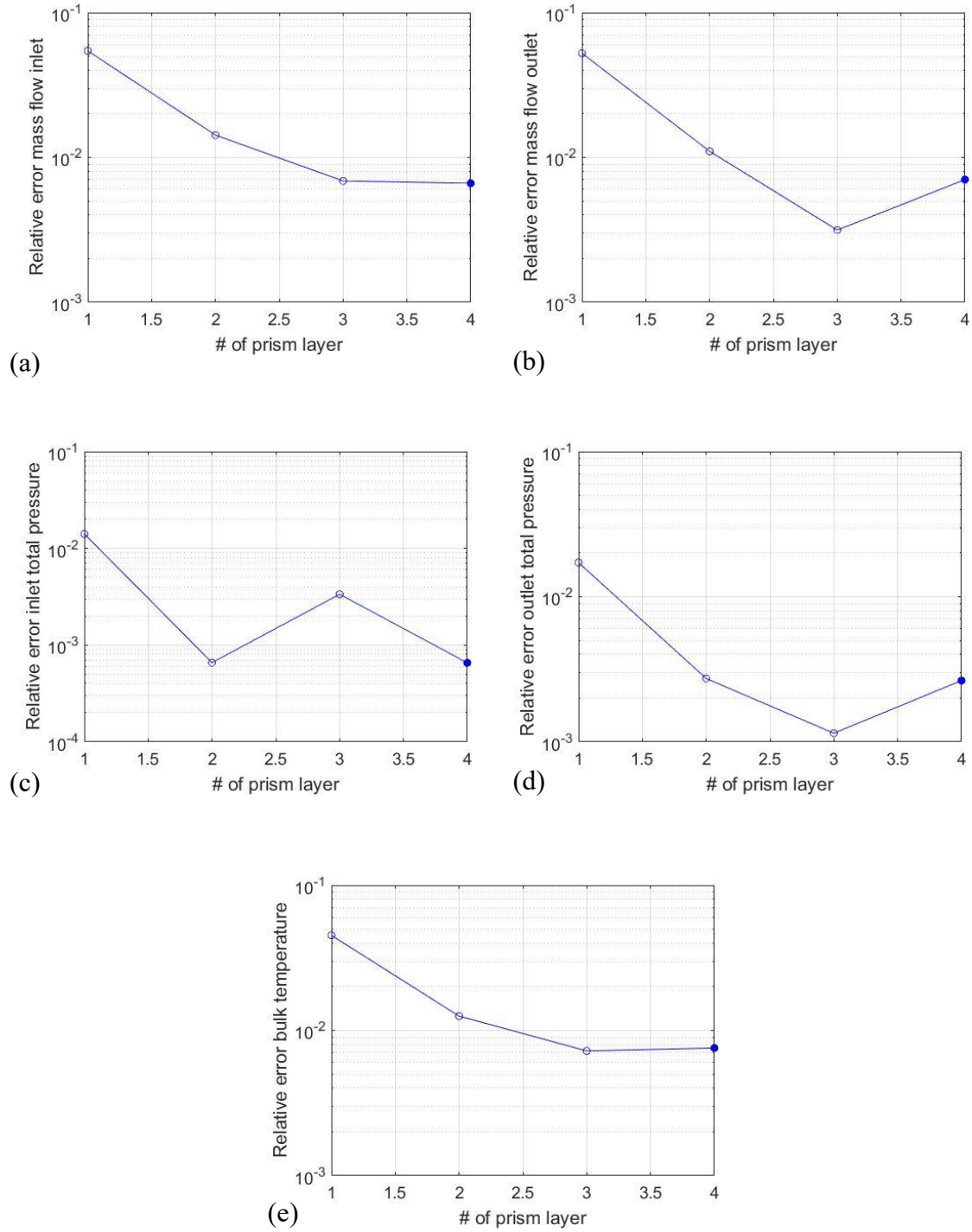


**Figure 5.4:** Relative error plots with respect to five prism layers simulation, for many prism layers values; error evaluated for a) inlet mass flow, b) outlet mass flow, c) inlet absolute total pressure, d) outlet absolute total pressure, e) outlet bulk temperature; all plots are in semi-log scale. Marked value is relative error value for the adopted number of prism layers.

Number of prism layers adopted is four: this because, all relative errors with respect to the five prism layers simulation are below 1e-02. Moreover, according to [Figure 5.4](#): relative error with respect to five prism layers simulation for inlet and outlet total pressure is quiet low; on the other hand. percentage difference between inlet and outlet mass flow is larger with respect to other simulations but is expected to decrease when adopting finer mesh. Five prism layers simulation is characterized by anomalous value of bulk outlet temperature, so it wasn't considered. In the end, simulations with number of prism layers less than four are characterized by high error content: that's why this choice has been made.

### 5.1.2 Polyhedral Meshing: Base Size Sensitive Analysis

Determined optimal number of prism layers, analysis proceed on finding optimal value of cells for a mesh with polyhedral cells. In order to do that, many simulations have been carried on, changing base size and performing error control for each monitor. Simulation stopped after 20'000 iterations if all residuals are below 1e-03; otherwise, simulation is stopped after 25'000 iterations. In this study, relative error was calculated with respect to "exact" solution according to Richardson extrapolation: we consider a generic quantity  $\phi$ , evaluated for three different mesh size ( $h, 2h, 3h$ ). Ratio between one mesh size and the successive (coarser) one is  $r = 2$ . Assuming that meshes are fine enough to suppose a monotone convergence, the following parameter can be calculated:

$$p = \frac{\log\left(\frac{\phi_{2h} - \phi_{4h}}{\phi_h - \phi_{2h}}\right)}{\log(r)} \quad (5.1)$$

Then, absolute error with respect to finest grid is:

$$\varepsilon_h \approx \frac{\phi_h - \phi_{2h}}{r^p - 1} \quad (5.2)$$

Thus, relative error can be calculated with respect to expected exact solution according to Richardson, where  $\phi_{Richardson} = \phi_h + \varepsilon_h$ .

Results of this analysis are present in [Table 5.2](#): although mesh with 0.08 mm base size is very fine, still monitors values are much different with respect to Richardson extrapolated exact value

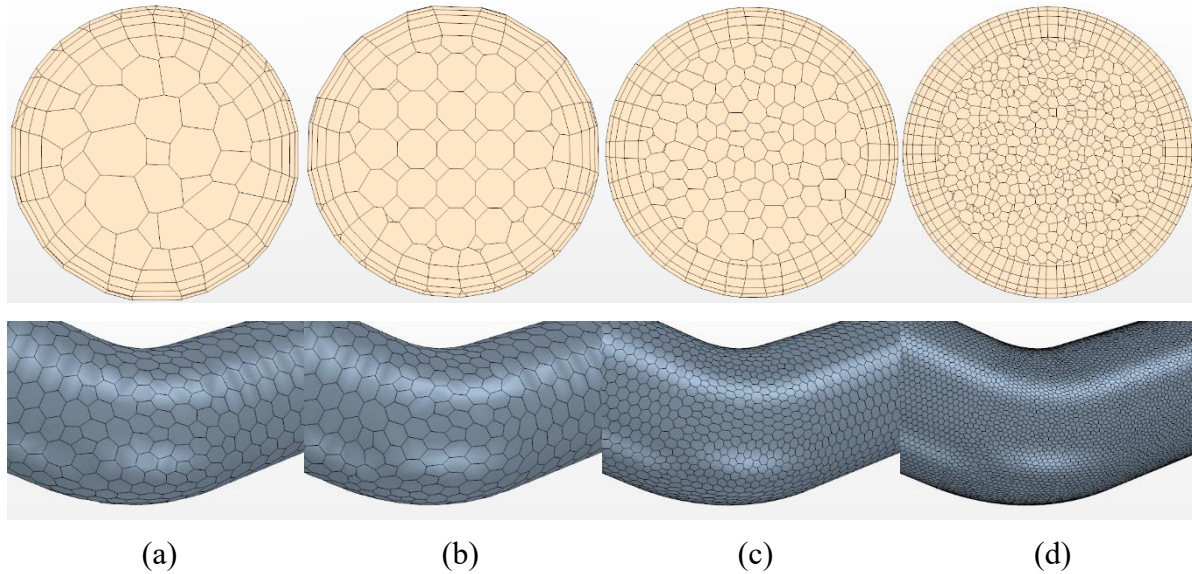


*Figure 5.5. Cross section view (top) and elbow detail (bottom) for polyhedral mesh with base size: a) 0.64 mm, b) 0.32 mm, c) 0.16 mm, d) 0.08 mm.*

Base Size [mm]	Cells	$\dot{m}_{in}$ [kg/s]	$\dot{m}_{out}$ [kg/s]	$\Delta\dot{m}$ [%]	$p_{in}$ [bar]	$p_{out}$ [bar]	$\Delta p$ [bar]	$T_{bulk}$ [K]
0.64	97159	3.414	3.439	0.732	8.89	7.50	1.39	767.48
0.32	117622	3.427	3.450	0.685	8.90	7.50	1.40	767.08
0.16	413770	3.590	3.616	0.739	9.01	7.51	1.49	762.21
0.08	3174590	3.676	3.686	0.275	9.06	7.54	1.52	760.55
Richardson	$\infty$	3.775	3.738	0.982	9.26	-	1.53	759.71

*Table 5.2: Results from sensitive analysis on the base size for polyhedral mesh*

Simulation with 0.04 mm base size is unfeasible due to huge amount of cells, so 0.08 mm base size seems to be a “bottle of neck” in term of hardware capability. With this limitation, it was not possible to have error decrease for outlet monitor pressure, so error control for this quantity was unfeasible. Conclusion of this analysis was that this meshing approach is not ensuring the required accuracy for a reasonable number of cells in which the domain is sub-divided. Polyhedral cells meshing strategy is appropriated when dealing with irregular geometry because it is more flexible and it offer higher capability to discretize the domain with high meshing quality.

On the other hand, number of faces for which conservation equation has to be computed is higher, so solution may be slower with respect to a more structured mesh; also a great CPU time for meshing procedure is needed because number of vertex that optimal location have to be found is higher.

As a conclusion, new meshing approach must be considered if higher accuracy of the solution is required with a reasonable number of cells.

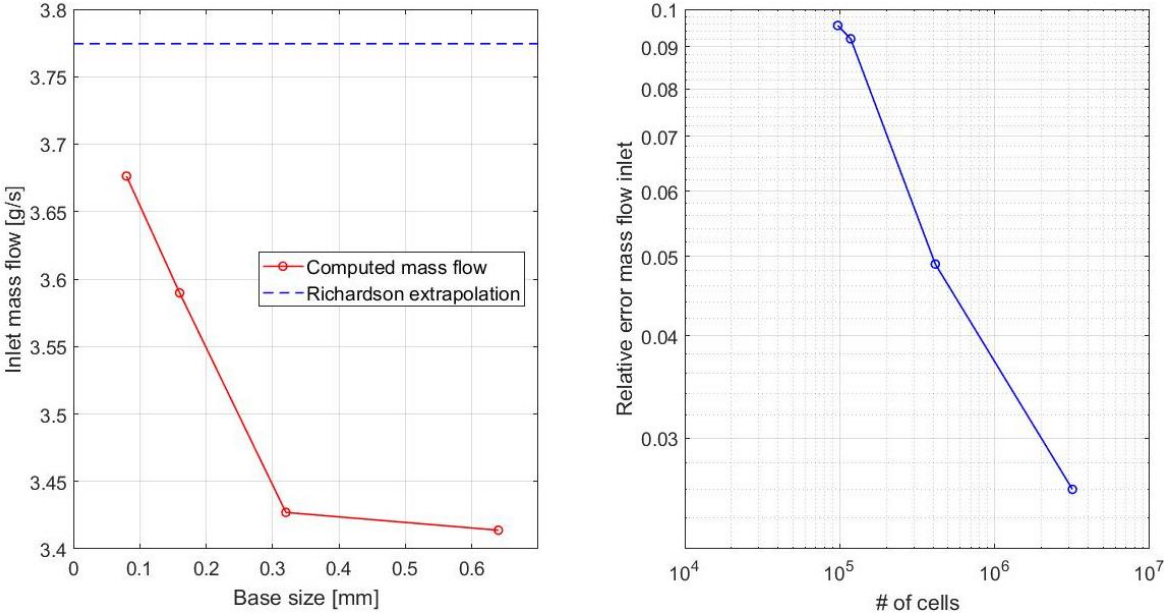


*Figure 5.6: Inlet mass flow related plots from grid independence analysis with polyhedral cells: computed value for each base size and extrapolated value (left), relative error with respect to extrapolated value as a function of number of cells in log-log scale (right)*

**5.1.3 Structured Meshing: Channel Layers and Base Size Sensitive Analysis**

According to the geometry of the system, because air flow has a preferential direction, a more structured cell in the channel region is advisable. *Star-CCM+* models library present a meshing model which is called “*Generalized Cylinder*”: the software automatically recognize portion of the domain that are semi-cylindrical, and uses a special cell’s shape: faces normal to flow direction are still polyhedral but each cell is elongated in flow direction; that’s why, making a section with a plane that passes in cylinder axis, cells look like rectangles. This meshing approach may accelerate convergence of the solution; moreover, meshing procedure is less

CPU demanding and number of cells is expected to decrease with respect to polyhedral meshing approach.

A new sensitive analysis has been carried on with this new meshing approach, keeping constant all meshing parameters concerning inlet and outlet control volumes as well as number of prism layers in channel region. This time, parameters that affects mesh size are:

- Number of layers in which channel region is sub-divided.
- Base size of each cell.

First, optimal value of channel layers has been derived, performing analysis with fixed base size cells in channel region (0.16 mm). Results are presented in [Table 5.3](#): optimal number of channel layers is 700; this because for a further increase of layers it is not possible to appreciate modification of monitors values.

Simulation with 600 channel layers has anomalous value of bulk outlet temperature, while 800 channel layers simulation has higher percentage difference between mass flow at inlet and outlet. Simulation with 500 channel layers or less have higher error content so they are not considered. All the relative error with respect to 800 channel layers simulation are equal or below  $5e-03$  so they are one order of magnitude less than error related to base size discretization of the previous study.

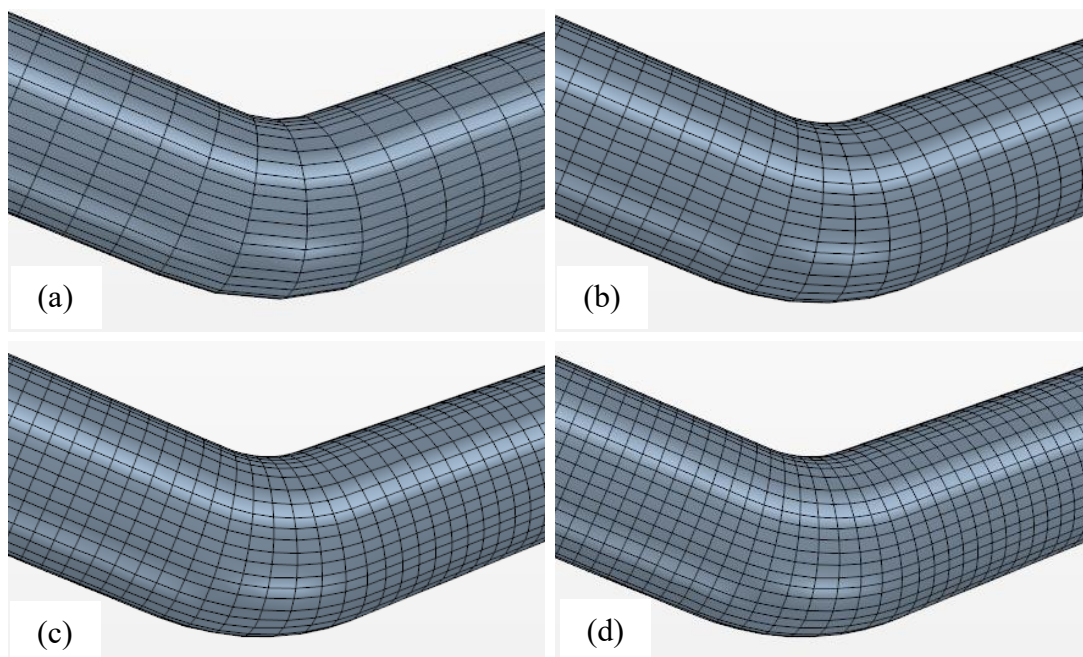


*Figure 5.7: Elbow detail for a structured mesh with a) 300 channel layers, b) 500 channel layers, c) 700 channel layers, d) 800 channel layers.*

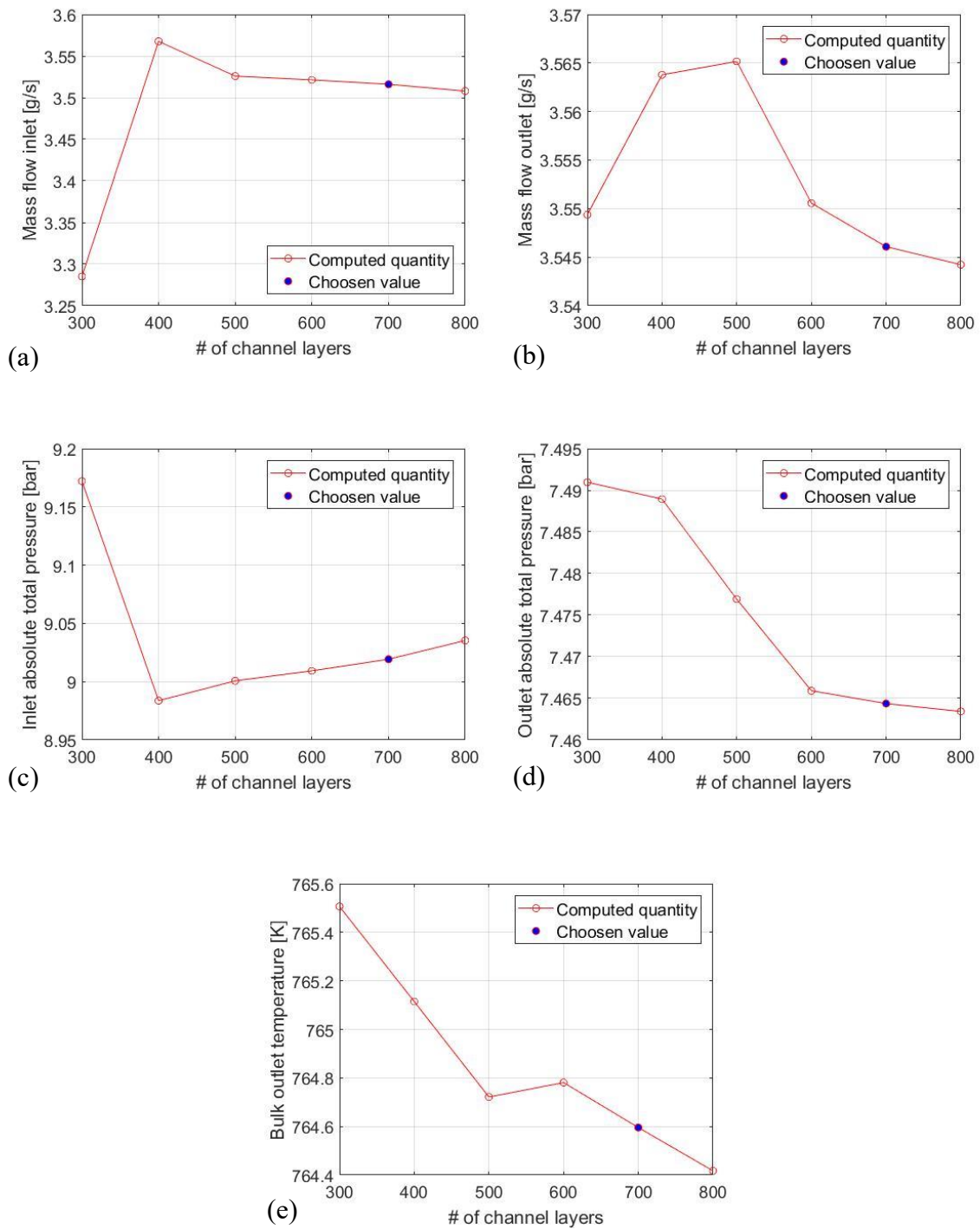


**Figure 5.8:** Computed quantities for each monitor and their extrapolated value, as a function of number channel layers in a structured mesh; a) inlet mass flow, b) outlet mass flow, c) inlet absolute total pressure, d) outlet absolute total pressure, e) outlet bulk temperature; Marked value is the monitor value for the adopted number of channel layers.

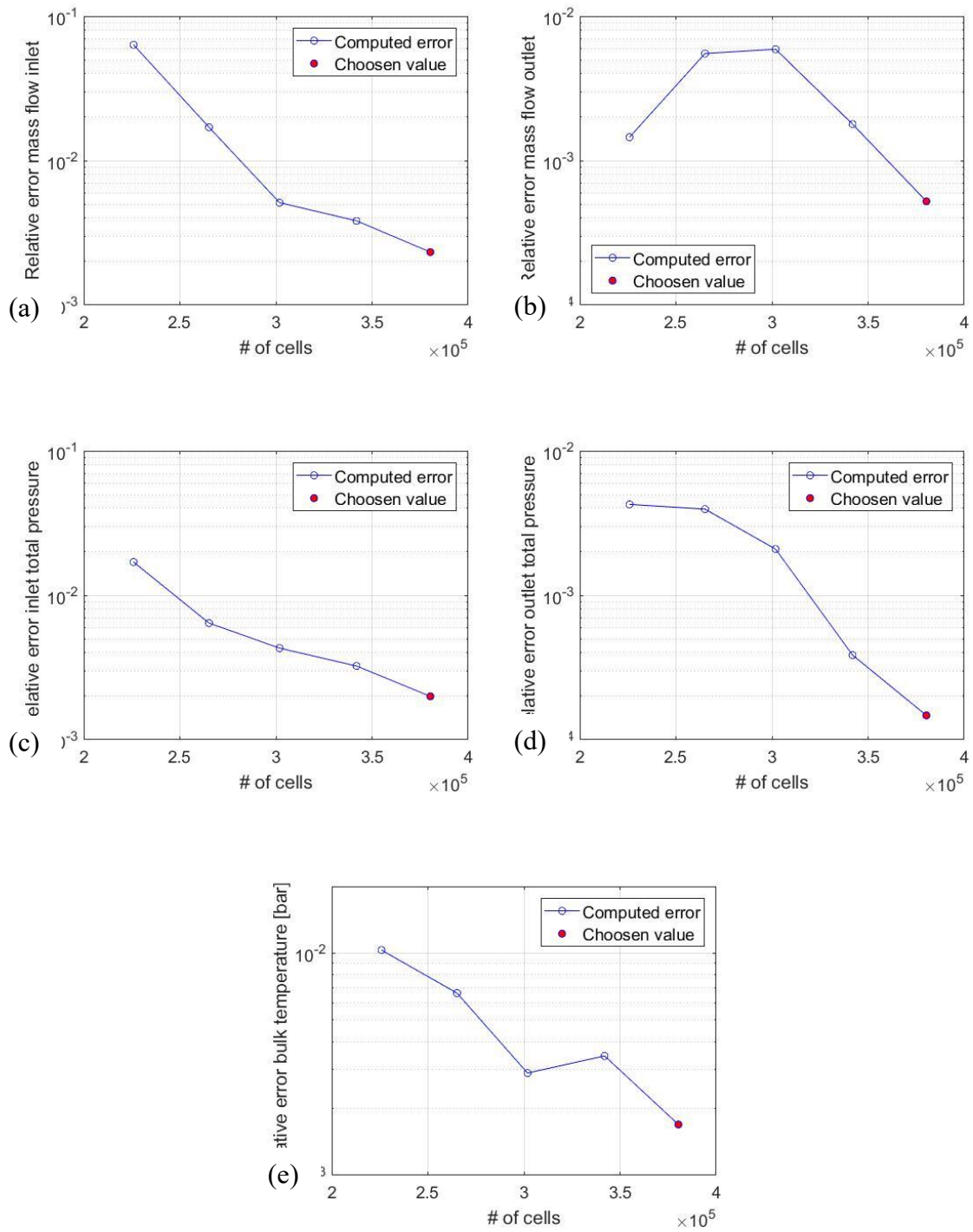


**Figure 5.9:** Relative error plots with respect to 800 channel layers simulation, for many channel layers values; error evaluated for a) inlet mass flow, b) outlet mass flow, c) inlet absolute total pressure, d) outlet absolute total pressure, e) outlet bulk temperature; all plots are in semi-log scale. Marked value is relative error value for the adopted number of channel layers.

Channel Layers	Cells	$\dot{m}_{in}$ [g/s]	$\dot{m}_{out}$ [g/s]	$\Delta\dot{m}$ [%]	$p_{in}$ [bar]	$p_{out}$ [bar]	$\Delta p$ [bar]	$T_{bulk}$ [K]
300	225870	3.285	3.549	8.042	9.17	7.49	1.68	765.51
400	265153	3.568	3.564	0.109	8.98	7.49	1.49	765.11
500	301868	3.526	3.565	1.115	9.00	7.48	1.52	764.72
600	341931	3.521	3.551	0.830	9.01	7.47	1.54	764.78
700	380319	3.516	3.546	0.854	9.02	7.46	1.55	764.6
800	418707	3.508	3.544	1.035	9.04	7.46	1.57	764.42

*Table 5.3: Results from sensitive analysis on the number of channel layers for a structured mesh, highlighted line is the chosen one.*

Defined optimal number of channel layers, sensitive analysis on base size has been carried on: three different meshes size was proved with fixed number of channel layers. With generalized cylinder approach it was possible to perform a simulation with 0.04 mm base size, which was unfeasible with previous meshing procedure. In the end, base size adopted is 0.16 mm: accuracy of the solution is not so different with respect to polyhedral meshing approach with same base size, but this method is presenting many advantages. With this combination of number of channel layers and base size dimension, each cell in channel region is characterized by aspect ratio of about 1.675:1 between elongated side and base size normal to flow direction, which seems to be appropriate for this flow field. Meshing procedure is less CPU demanding so it is expected to be easier to implement for geometry with higher number of channels. Error is better managed because its decrease is reached for all monitors: this mean that Richardson extrapolation has been calculated for all the controlled physical quantities and all the relative errors are computed with respect to extrapolated exact solution.

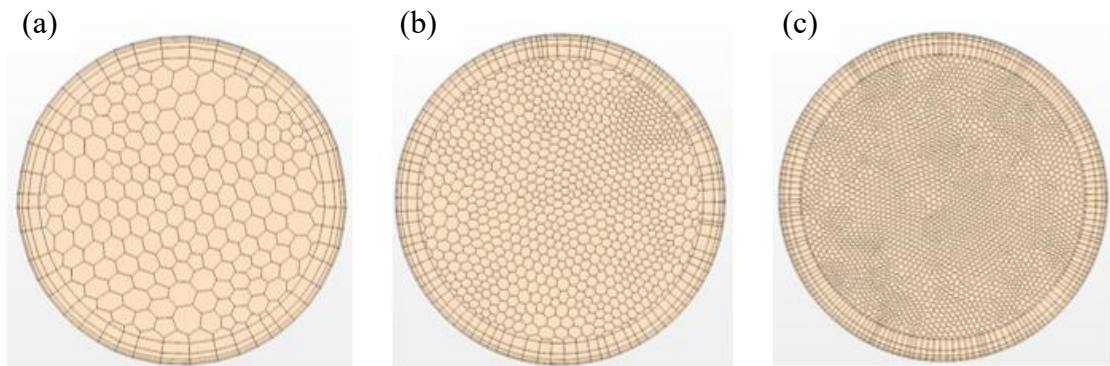


*Figure 5.10: Cross section in channels region with magnification of the three base sizes adopted during sensitive analysis for structured mesh; a) base size: 0.16 mm, b) base size: 0.08 mm, c) base size: 0.04 mm.*

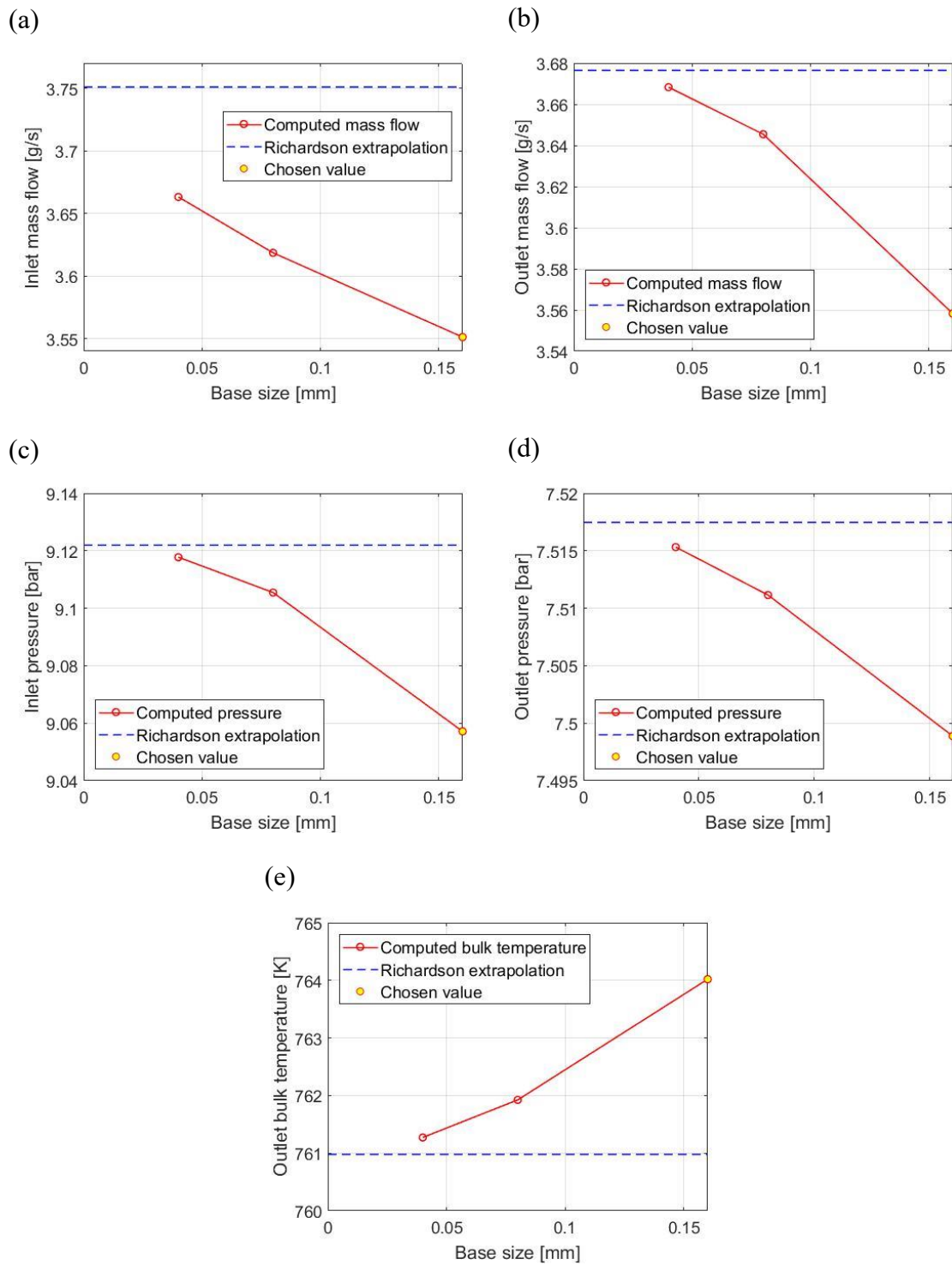


**Figure 5.11:** Computed quantities for each monitor and their extrapolated value as a function of the base size values; simulations with structured mesh and 700 channel layers; a) inlet mass flow, b) outlet mass flow, c) inlet absolute total pressure, d) outlet absolute total pressure, e) outlet bulk temperature; Marked value is the monitor value for the adopted mesh base size.

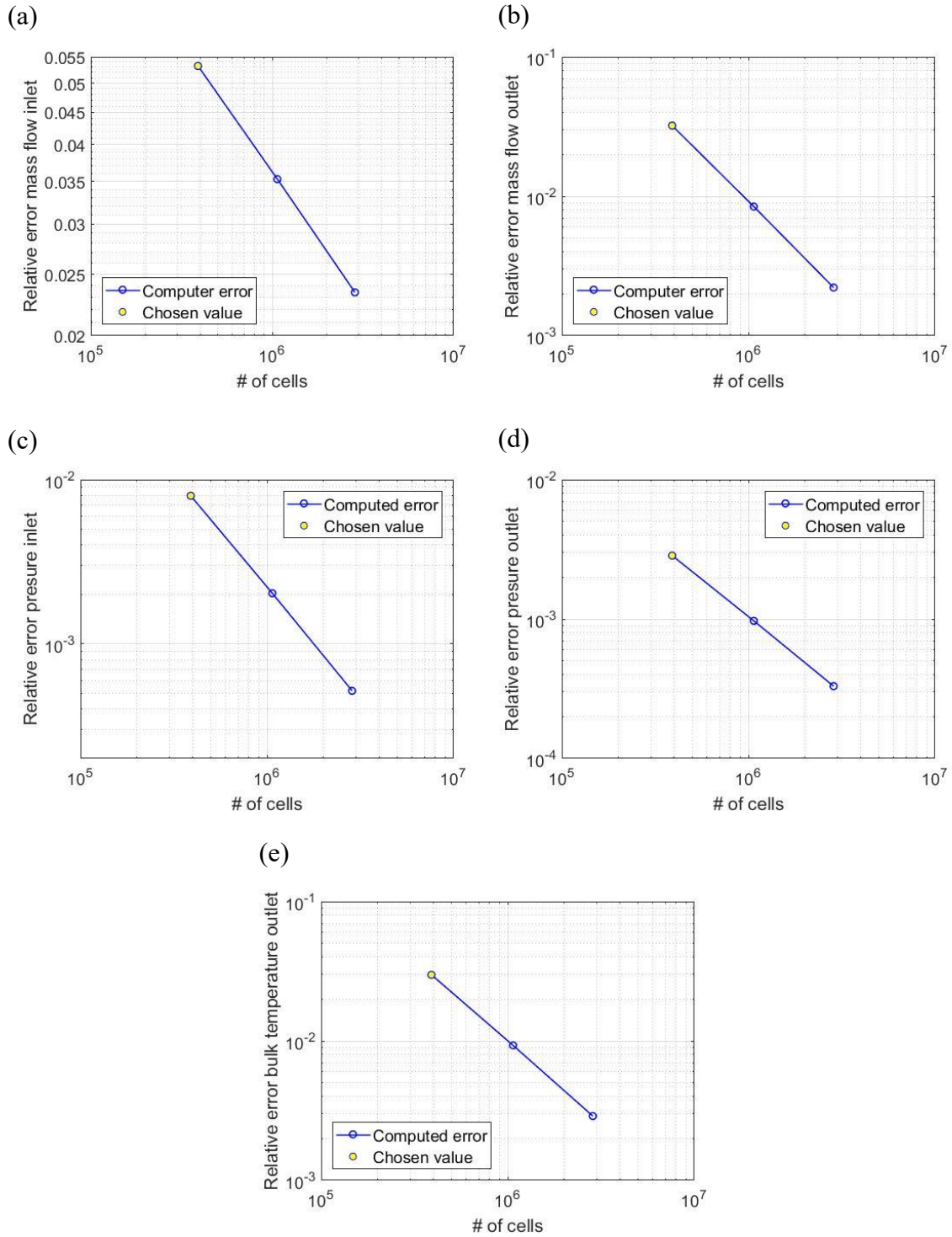


**Figure 5.12:** Relative error plots with respect to Richardson extrapolated value, as a function of the number of cell of each simulation with different base size in a structured mesh; error evaluated for a) inlet mass flow, b) outlet mass flow, c) inlet absolute total pressure, d) outlet absolute total pressure, e) outlet bulk temperature; all plots are in semi-log scale. Marked value is relative error value for the adopted mesh base size.

base size [mm]	# of cells	$\dot{m}_{in}$ [g/s]	$\dot{m}_{out}$ [g/s]	$\Delta\dot{m}$ [%]	$p_{in}$ [bar]	$p_{out}$ [bar]	$\Delta p$ [bar]	$T_{bulk}$ [K]
0.16	390043	3.551	3.558	0.199	9.06	7.50	1.56	764.02
0.08	1068495	3.618	3.645	0.744	9.11	7.51	1.59	761.92
0.04	2859571	3.663	3.668	0.142	9.12	7.52	1.60	761.27
Richardson	$\infty$	3.751	3.676	2.025	9.12	7.52	1.60	760.98

Table 5.4: Results from sensitive analysis on the base size of each channel layer for a structured mesh.

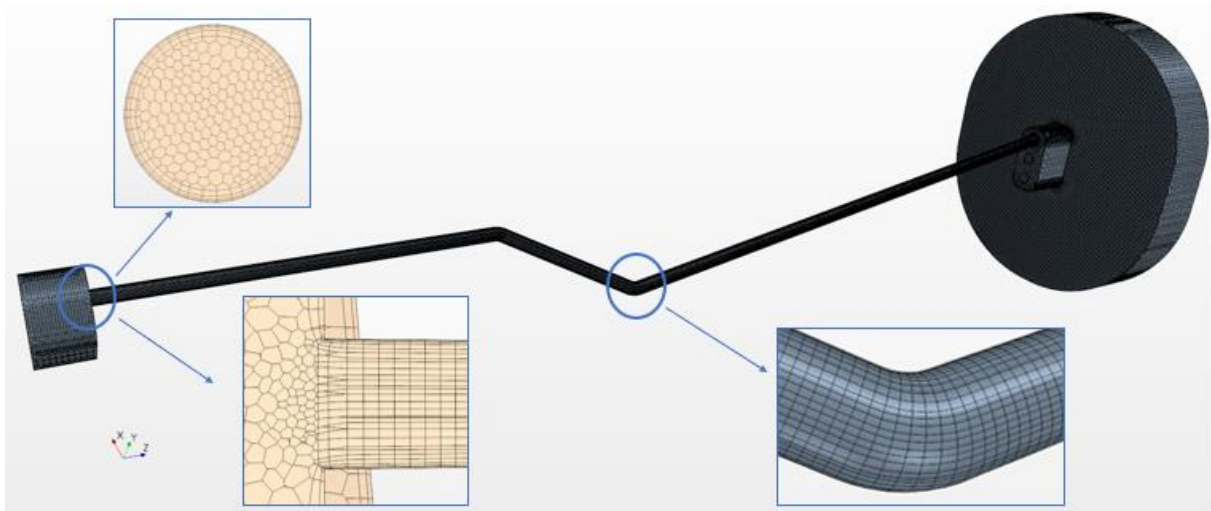
#### 5.1.4 Final Results and Comments on Grid Independence Analysis

Thanks to this analysis it was possible to completely study physical phenomenon behind real case fluid motion inside rotor cooling channel and it was found best mesh in term of trade-off between computational cost and accuracy of the results. Consistency has been proved: it means that discretization error decreases as mesh gets finer. Discretization error will be fundamental on managing accuracy also for following simulations, in which more channel will be solved together: we can reasonably say that, relative error for each of the computed monitor in channel #3 can be extended to all the other channels, considering similarity in the geometry and same kind of boundary conditions.

In [Table 5.5](#) are presented monitors values for the simulation with adopted mesh and new value of heat source and inlet temperature ( $\dot{Q} = 0.824 \text{ kW}$ ,  $T_{in} = 529.44 \text{ K}$ ): differences can be noticed between CFD and PH4165 data, even if uncertainty is taken into account. Westinghouse developed software seems to roughly over-estimate coolant mass flow for that pressure drop but, on the other hand, CFD simulation is modelling two local pressure drops (inlet restriction and outlet expansion) that are not considered by PH4165 but are necessary in order to properly set boundary conditions. Because of reduced mass flow,  $T_{bulk}$  at channel's outlet is higher according to CFD simulation.

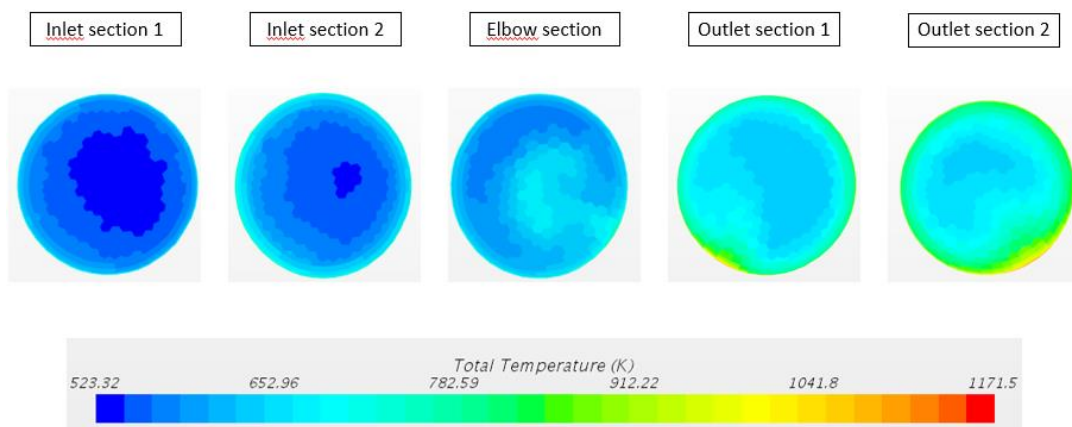
	Computed value	Uncertainty	PH4165
$\dot{m}_{in}$ [g/s]	3.684	$\pm 0.196$	3.882
$\dot{m}_{out}$ [g/s]	3.700	$\pm 0.119$	3.882
$p_{in}$ [bar]	9.128	$\pm 0.06$	9.55
$p_{out}$ [bar]	7.559	$\pm 0.02$	6.38
$\Delta p$ [bar]	1.531	$\pm 0.04$	3.17
$T_{bulk}$ [K]	738.664	$\pm 2.75$	728.89

Table 5.5: Computed monitors values from CFD and their uncertainty based on grid sensitive analysis for a single cooling channel geometry; comparison with company's software output data.



**Figure 5.13:** Final adopted mesh, with details magnification of cross section and axial section in the channel entry region, and mesh quality in elbow portion of the channel.

As a result of simulation with selected mesh, complete maps of many physical quantities have been obtained, in order to fully understand air flow behaviour inside such a narrow channel. Great interest is reserved to the *elbow* region, which is the portion of the channel with geometry variation: it is possible to notice in [Figure 5.14](#) that sudden air flow direction variation determines local stagnation; which means that local mass flow is reduced. As a consequence of that, capability to remove heat thanks to advection contribution is reduced, so local hot spot formation is present. It's also interesting to notice that hot spot is still evident also in outlet portion of the domain, but it's changing its position as air progresses inside the channel. This phenomenon is surely affecting heat transfer property of the channel, which is of great interest in order to fully understand performance of the cooling system.



**Figure 5.14:** Total temperature maps for the five sections of interest and their colour map; a) inlet section #1, b) inlet section #2, c) elbow section, d) outlet section #1, e) outlet section #2

Five sections of the channels were considered: two of them are located in entry region, before channel's geometry variation, one section is located in the mid of the elbow and other two sections are located in outlet region. For each of the section it was evaluated the mass flow averaged temperature, or *bulk* temperature  $T_{bulk}$ , and the line average temperature on the external surface of the channel, which is called  $T_{wall}$ . Known the heat flux value per unit of channel's external surface  $q''$ , local value of the convective heat transfer coefficient has been calculated according to *Newton's law*:

$$q'' = h(T_{wall} - T_{bulk}) \quad (5.3)$$

And considering an average value of the air thermal conduction  $\lambda$  (which is in principle a function of temperature), it was possible to calculate also local value of the *Nusselt number*:

$$Nu = \frac{hD_{eq}}{\lambda} \quad (5.4)$$

Where  $D_{eq}$  is the hydraulic equivalent diameter, but in our case is exactly the external diameter of the channel. In [Table 5.6](#) are reported all these value for the five section of interest plus inlet and outlet sections: it is interesting to notice that, although hot spot formation is present in elbow section, due to increased vorticity, average air value on external surface is reduced, so we have local better performance regarding heat transfer coefficient; this parameter is always locally higher than  $h = 1891.69 \text{ W/m}^2/\text{K}$ ; which is average value estimated by *Ethos* engineers, derived from PH4165 software.

	z [mm]	$T_{wall}$ [K]	$T_{bulk}$ [K]	h [ $\text{W/m}^2/\text{K}$ ]	Nu
<b>Inlet section</b>	0.00	694.63	530.79	3420.84	121.51
<b>Nu section inlet 1</b>	21.02	742.93	554.83	2979.72	105.85
<b>Nu section inlet 2</b>	42.03	793.40	579.06	2614.85	92.88
<b>Nu section elbow</b>	74.08	761.98	615.78	3833.51	136.17
<b>Nu section outlet 1</b>	122.97	903.47	669.55	2395.93	85.11
<b>Nu section outlet 2</b>	156.06	969.02	704.98	2122.70	75.40
<b>Outlet section</b>	187.73	1005.76	738.56	2097.61	74.51

*Table 5.6: Local heat transfer coefficient and Nusselt number for seven sections of interest of the cooling channel.*

Starting from this set of data, it has been possible to estimate values of:

- Wall temperature ( $T_{wall}$ );
- Bulk temperature ( $T_{bulk}$ );
- Heat transfer coefficient ( $h$ );

as a function of the axial coordinate ( $z$ ). Functions has been obtained from data interpolation of these nodes; for bulk temperature a lagrangian interpolant function has been used, for the other two quantities a cubic spline interpolant function is needed in order to avoid Runge's phenomenon.

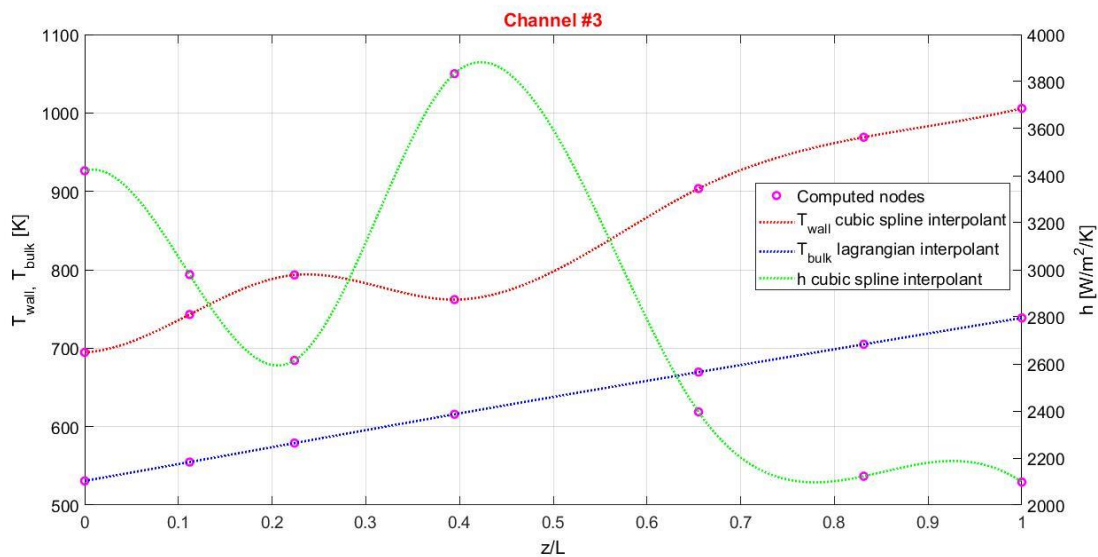


**Figure 5.15:** Surface average temperature ( $T_{wall}$ ), mass flow average air temperature ( $T_{bulk}$ ) and heat transfer coefficient ( $h$ ) linked to axial distance normalized with respect to total channel's length ( $z/L$ ) according to their interpolant function.

## 5.2 First Group Geometry

Before analysing the complete system, an intermediate step has been considered: in this second part of the study of radial holes cooling channel geometry, simulations of the first group of channels are presented. Main difference with previous geometry is that inlet vane is shared by three different channels: this condition will determine modification in the flow dynamic of the system and induce also some troubles concerning stability of the solution. Same geometry has

been studied in steady state and transient conditions, these two simulations are providing very similar results, but with different computational effort.

Physical models and boundary conditions imposed are the same of the single channel geometry; mesh adopted is the same of the previous geometry, but number of channel layers has been decreased from 700 to 500, in order to reduce size of the numerical simulation. Number of cell reduction is surely affecting accuracy of the solution, but thanks to grid size sensitive analysis, we can control error and estimate uncertainty related to each monitor result. Some mesh refinement at control volume region has been considered: this will be motivated according to residuals trend that will be described in the following sections of the present study; in any case, increase of number of cells is negligible.



*Figure 5.16: Geometry adopted for first group CFD analysis*

### *5.2.1 Steady-state Analysis*

Steady state simulation was affected by instability and, in many cases, simulations failed due to divergence. Some numerical control was necessary: a linear ramp for both CFL number and UR factor for k- $\epsilon$  model has been set, in order to have a proper initialization of the simulation and avoid residual fluctuation during initial iterations, which are typically very difficult in case of complex geometry, that's why they need a special treatment.

Residuals of steady-state simulation are showed in [5.17](#): although simulation converged, it can be noticed that energy residuals are above threshold value of  $5e-03$  so, generally speaking,

accuracy of the solution may also be affected by convergence error, which is the difference between exact and iterative solution of discretised equations that describe air flow physics. Moreover, considering that  $tdr$  residuals are higher than one, turbulent model equation concerning  $\varepsilon$  conservation is not converged.

Theoretically speaking, this would reduce decrease of reliability of these results, even if simulations ends without any error. At the end of the analysis it was investigated which are cells with high error content (residuals above threshold value) and, it was found that they are all located in control volume regions (both at inlet and outlet). This is the main reason why a meshing refinement has been considered in entry region: this is expected to reduce residuals values during initial iterations and increase stability of the simulation. Residuals value may be further decreased considering mesh refinement or unsteady simulation. Considering that these regions are necessary just in order to properly impose boundary conditions, high residuals values may be accepted, so reliability of results may be considered as unchanged.

Monitor results of steady state analysis are presented in [Table 5.7](#): uncertainty of each measurement has been evaluated considering as constant the relative error for each monitor obtained from grid size sensitive analysis. Total relative error is calculated as summation of relative error connected to base size discretization and relative error related to channel layers sub-division; the latter is no more negligible due channel layers reduction from 700 to 500 so uncertainty related to each computed quantity increases. It can be noticed that some differences between single channel and three channels analysis stands: this because air from inlet control volume must split into each of the three channel and this new mechanism is surely affecting air fluid dynamic.

	Channel #					
	1		2		3	
	Computed	Uncertainty	Computed	Uncertainty	Computed	Uncertainty
$\dot{m}_{in}$ [g/s]	3.629	± 0.212	3.738	± 0.218	3.850	± 0.225
$\dot{m}_{out}$ [g/s]	3.691	± 0.140	3.789	± 0.144	3.723	± 0.142
$p_{in}$ [bar]	9.17	± 0.10	9.15	± 0.10	9.15	± 0.10
$p_{out}$ [bar]	7.41	± 0.03	7.40	± 0.03	7.47	± 0.03
$\Delta p$ [bar]	1.77	± 0.11	1.74	± 0.11	1.68	± 0.10
$T_{bulk}$ [K]	741.52	± 3.06	737.00	± 3.00	734.14	± 2.95

*Table 5.7: Monitors results with their absolute uncertainty, obtained from steady-state simulation*

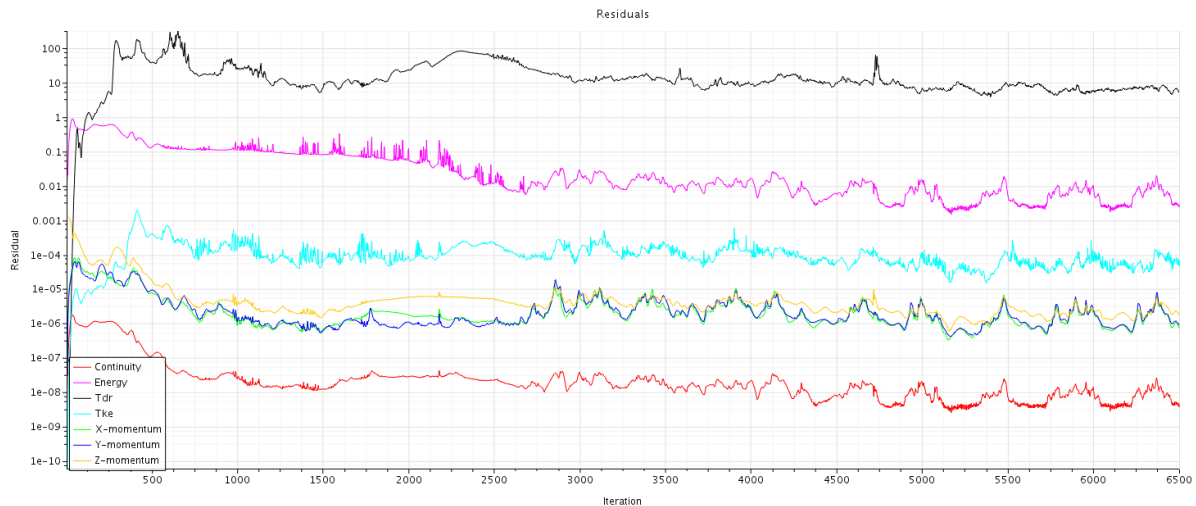


Figure 5.17: Steady-state analysis residuals plot for three channels geometry.

### 5.2.2 Transient Analysis

After steady-state analysis, a new simulation with same physical models but transient analysis has been set. Unsteady solver adopted is the coupled implicit one: it was imposed a time-step of  $5e-06$  second, and a number of iterations per each time step equal to five. Number of iterations per time step should be higher if a comprehensive analysis as a function of time is requested but, in our case, just information at completed transient are needed. Uniform static pressure in the entire domain equal to  $p = 9.55 \text{ bar}$  is set as initial condition; at following time-step it happens a step-variation of outlet pressure ( $p_{outlet}^{t=\Delta t} = 6.38 \text{ bar}$ ). Initial temperature is set as equal to inlet temperature of the channel.

Simulation is characterised by high residuals oscillation, which is common for a transient simulation. Main advantages of this analysis with respect to steady-state one is that its convergence is reached after just 5000 iterations; this correspond to a total physical time of 5 milli-second after which transient is fully concluded. Still high residuals value characterises this simulation but, also in this case, cells with high error content are located only in inlet and outlet vane. Matching between steady state and transient monitor results is almost perfect: this fully validate previous results.

Because of faster convergence and less numerical control required, transient simulation is preferred with respect to steady state, and it has been used also for fifteen channels simulation.

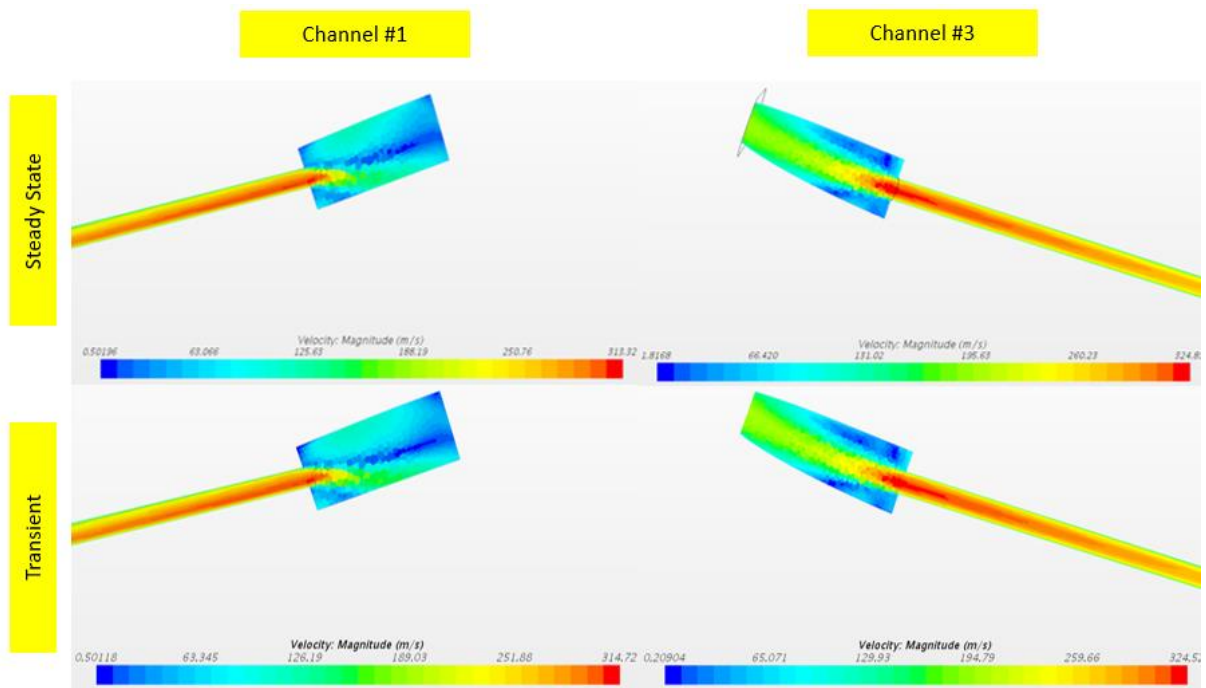


*Figure 5.18: Comparison of velocity magnitude profile at outlet of channel #1 and #3 for both steady-state and implicit unsteady simulation.*

### 5.3 Fifteen Channels Geometry

Simulation with complete geometry is characterized by great computational effort in order to completely develop the analysis. Mesh adopted is the same of the first group analysis: 500 layers per channel and base size of 0.16 mm; result of this is a mesh with total number of cells equal to 4'441'285. Simulation is characterized by four different regions: this is because a single channel group is not sharing any flow path with other groups, so solution of each region is computed separately, increasing computational cost of the analysis. It was figured out that steady state simulation requires larger number of iterations before convergence, moreover numerical control of many parameters was necessary in order to properly reach convergence. In the end, all the results that will presented are from transient simulation, for which convergence is reached in a relatively low number of iterations and with no numerical control needed but with higher residuals oscillations, which is usual for an unsteady analysis. Solver and turbulence model are unchanged with respect to previous simulations, analysis is marching in time with  $\Delta t = 5 e - 06 s$ ; per each time step just five iterations are performed

due to lack of interest of transient behaviour. Maximum time step is set equal to 0.01 s but simulation was stopped after 0.007 s because convergence has been already reached.

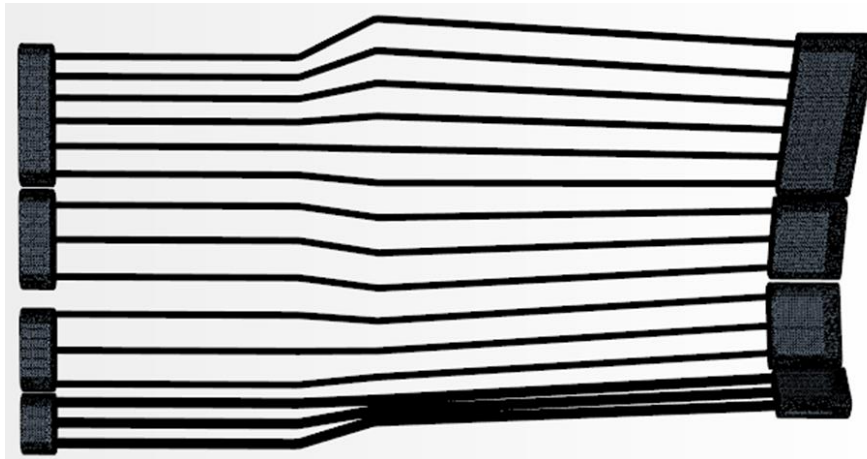


*Figure 5.19: Mesh adopted for 15 channels analysis: mesh refinement can be noticed at outlet manifolds, where pressure wave starts to propagate during initial iterations, causing instability of the solution.*

Boundary conditions of fifteen channels analysis are reported in [Table 5.8](#); initial pressure is set equal to  $p_{total,inlet}$  along the entire domain, as well as initial temperature which is set equal to  $T_{total,inlet}$ . At successive time-step, total outlet pressure changes to its steady state value, so each channels group experiences a step variation of this physical quantity. This approach is expected to increase convergence of the solution.

According to residuals plot, also in this case convergence error for turbulent dissipation rate ( $\epsilon$ ) is very high. Main difference with respect to previous simulations is that cells with high tdr values are located also in channels regions. This is surely reducing results reliability: convergence error may be reduced increasing number of cells, that is unfeasible in our case because of huge computational cost that would be needed.

In the end, this high error source can be accepted, regarding the fact that there is a good matching between monitor values of the present simulation and previous ones.

CHANNELS #															
	1	2	3	4	5	6	7	8	9	10	11	12	13	14	15
$P_{static,inlet}$ [bar]	9.55	9.55	9.55	9.55	9.55	9.55	9.55	9.55	9.55	9.55	9.55	9.55	9.55	9.55	9.55
$P_{total,inlet}$ [bar]	9.55	9.55	9.55	9.55	9.55	9.55	9.55	9.55	9.55	9.55	9.55	9.55	9.55	9.55	9.55
$P_{total,outlet}$ [bar]	6.38	6.38	6.38	5.89	5.89	5.89	5.39	5.39	5.39	4.90	4.90	4.90	4.90	4.90	4.90
$T_{total,inlet}$ [K]	529.44	529.44	529.44	529.44	529.44	529.44	529.44	529.44	529.44	529.44	529.44	529.44	529.44	529.44	529.44
$T_{total,outlet}$ [K]	728.89	728.89	728.89	830.00	830.00	830.00	855.56	855.56	855.56	855.56	855.56	855.56	855.56	855.56	855.56
$Q_{channel}$ [kW]	0.824	0.824	0.824	0.489	0.489	0.489	0.532	0.532	0.532	0.552	0.552	0.552	0.552	0.552	0.552
	GROUP 1			GROUP 2			GROUP 3			GROUP 4					

*Table 5.8: Boundary conditions of fifteen channels analysis, according to PH4165 software*

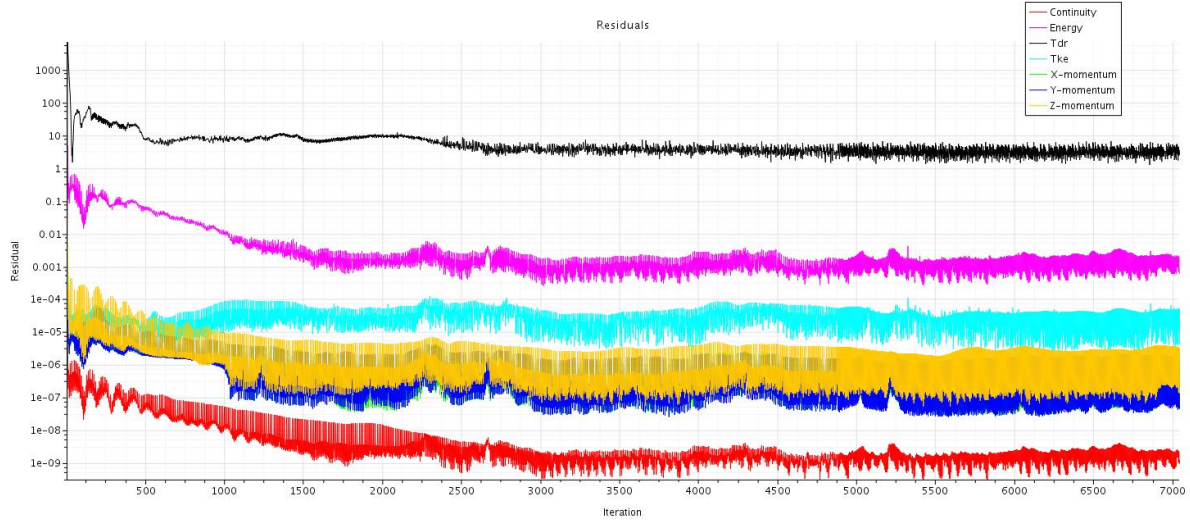


Figure 5.20: Residuals plot of unsteady fifteen channels geometry analysis.

In [Table 5.9](#) are reported all monitors results for each channel; uncertainty of the measurement is calculated according to relative error obtained from one channel sensitive analysis. Uncertainty related to mass flow measurement is lower for channels belonging to group 2, 3 and 4: this is because computed value is little so uncertainty related to it it's also reduced. On the contrary, uncertainty related to bulk outlet temperature increases as channel diameter is reducing because relative error is calculated with respect to  $\Delta T = T_{bulk,outlet} - T_{inlet}$ , which is higher for group 2, 3 and 4 due to higher heat source values with respect to reduced mass flow.

channels #	$\dot{m}_{in}$ [g/s]		$\dot{m}_{out}$ [g/s]		$p_{in}$ [bar]		$p_{out}$ [bar]		$\Delta p$ [bar]		$T_{bulk}$ [K]		
	Computed	Uncertainty	Computed	Uncertainty	Computed	Uncertainty	Computed	Uncertainty	Computed	Uncertainty	Computed	Uncertainty	
GROUP 1	1	3.697	$\pm 0.216$	3.655	$\pm 0.139$	9.17	$\pm 0.10$	7.41	$\pm 0.03$	1.76	$\pm 0.11$	741.44	$\pm 3.06$
	2	3.790	$\pm 0.221$	3.742	$\pm 0.142$	9.15	$\pm 0.10$	7.41	$\pm 0.03$	1.73	$\pm 0.10$	737.06	$\pm 3.00$
	3	3.848	$\pm 0.225$	3.802	$\pm 0.145$	9.15	$\pm 0.10$	7.49	$\pm 0.03$	1.67	$\pm 0.10$	734.11	$\pm 2.95$
GROUP 2	4	1.257	$\pm 0.073$	1.242	$\pm 0.047$	9.26	$\pm 0.10$	6.96	$\pm 0.03$	2.30	$\pm 0.14$	888.87	$\pm 5.19$
	5	1.278	$\pm 0.075$	1.261	$\pm 0.048$	9.24	$\pm 0.10$	7.01	$\pm 0.03$	2.23	$\pm 0.14$	883.39	$\pm 5.11$
	6	1.257	$\pm 0.073$	1.246	$\pm 0.047$	9.26	$\pm 0.10$	7.00	$\pm 0.03$	2.26	$\pm 0.14$	887.53	$\pm 5.17$
GROUP 3	7	1.289	$\pm 0.075$	1.279	$\pm 0.049$	9.24	$\pm 0.10$	6.69	$\pm 0.03$	2.55	$\pm 0.15$	907.76	$\pm 5.46$
	8	1.284	$\pm 0.075$	1.271	$\pm 0.048$	9.24	$\pm 0.10$	6.69	$\pm 0.03$	2.55	$\pm 0.15$	909.50	$\pm 5.48$
	9	1.291	$\pm 0.075$	1.278	$\pm 0.049$	9.23	$\pm 0.10$	6.69	$\pm 0.03$	2.55	$\pm 0.15$	907.46	$\pm 5.45$
GROUP 4	10	1.329	$\pm 0.078$	1.315	$\pm 0.050$	9.22	$\pm 0.10$	6.45	$\pm 0.03$	2.77	$\pm 0.17$	911.00	$\pm 5.51$
	11	1.341	$\pm 0.078$	1.325	$\pm 0.050$	9.21	$\pm 0.10$	6.50	$\pm 0.03$	2.71	$\pm 0.16$	907.47	$\pm 5.46$
	12	1.333	$\pm 0.078$	1.318	$\pm 0.050$	9.21	$\pm 0.10$	6.47	$\pm 0.03$	2.74	$\pm 0.17$	909.40	$\pm 5.48$
	13	1.317	$\pm 0.077$	1.300	$\pm 0.049$	9.22	$\pm 0.10$	6.41	$\pm 0.03$	2.81	$\pm 0.17$	915.03	$\pm 5.56$
	14	1.294	$\pm 0.076$	1.276	$\pm 0.049$	9.24	$\pm 0.10$	6.36	$\pm 0.03$	2.88	$\pm 0.17$	921.30	$\pm 5.65$
	15	1.266	$\pm 0.074$	1.248	$\pm 0.047$	9.25	$\pm 0.10$	6.35	$\pm 0.03$	2.90	$\pm 0.18$	929.52	$\pm 5.77$

Table 5.9: Monitor results from fifteen channels unsteady simulation.

Fifteen channels study is completed with analysis of heat transfer properties of five channels of interest: behaviour of channels 2, 5 and 8 is expected to be similar for all channels of same group. Regarding group 4, both channels 12 and 15 has been considered, in order to appreciate

difference in heat transfer properties between almost a straight channel (# 12) and one with sudden geometry change. Seven sections have been considered for each channel: section at inlet and outlet of the channel, two sections in inlet portion of the channel (between inlet section and elbow portion), one section in elbow portion and other two sections in outlet portion.

For each section, following parameters have been considered:

- Line average temperature at channel surface ( $T_{wall}$ );
- Mass flow averaged air temperature ( $T_{bulk}$ );
- Convective heat transfer coefficient ( $h$ ), according to Newton's law;
- Nusselt number ( $Nu$ ), known hydraulic diameter of the channels and considering average value of thermal conductivity ( $\lambda$ ).

Each of this quantity can be expressed as a function of  $z$  coordinate, which is defined as distance between inlet section and section of interest along the axial profile of the channel.

Thus, a set of seven data for  $T_{wall}$ ,  $T_{bulk}$  and  $h$  is obtained: in order to obtain a local map of this quantity, data interpolation is needed. Both lagrangian and cubic spline interpolant method is used. first method is preferred due to its simplicity: interpolant is a polynomial function whom degree  $n \leq N - 1$ , where  $N$  is the number of nodes  $(x_i, y_i)$ . From this method, anomalous oscillation of the function may arise; this is called *Runge phenomenon* and it's the main limitation of lagrangian method with a set of data whom trend can be recognized as non-monotonic and error related to the interpolation increases as  $n$  increase [13]. In case of function oscillation, cubic spline interpolant is preferred: it consists of a piecewise interpolant cubic function. In order to have smooth function, also derivative continuity must be imposed: as a result, higher number of equations must be solved for a given set of  $n$  nodes with respect to lagrangian interpolant, so computational effort is higher.

Computed nodes and their interpolant functions are presented in following figures. As can be noticed, sudden geometry variation determines a reduction of  $T_{wall}$  and consequent  $h$  local increase. This can be appreciated for all channels except for channel #5, in which increased turbulence is less evident due to almost straight profile. Main difference between channel #12 and channel #15 is higher maximum value of  $h$  for the second one, determined by sudden geometry variation that is not present in first three channels of group 4.

Still some oscillation of  $h$  interpolant function is present in channel #8, although adoption of cubic spline method, but this can be justify considering  $T_{wall}$  trend, that is oscillating.

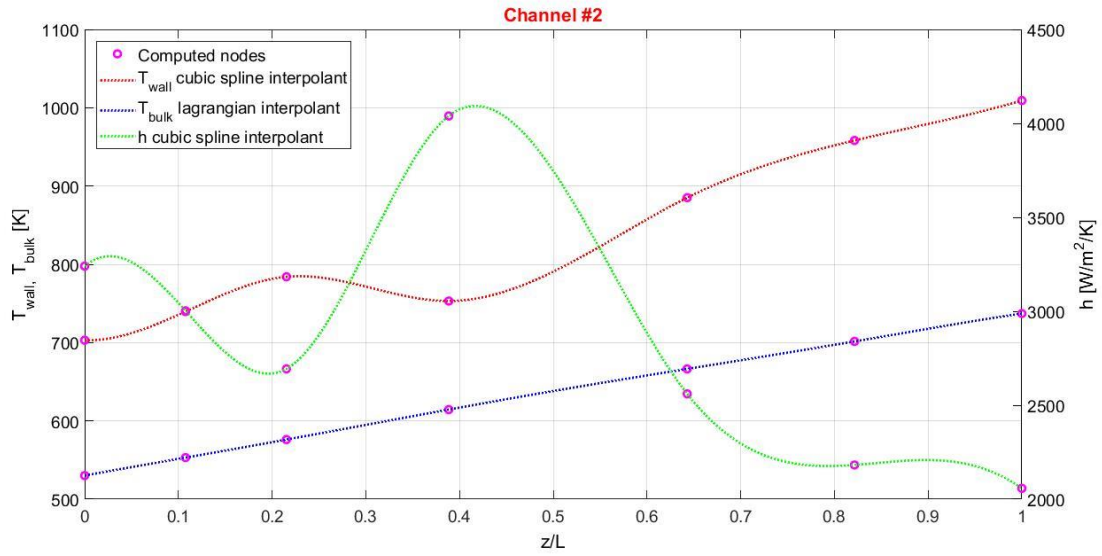


Figure 5.21: Computed nodes and interpolant functions for wall temperature ( $T_{wall}$ ), mass flow averaged temperature ( $T_{bulk}$ ) and heat transfer coefficient ( $h$ ) as a function of normalized axial distance ( $z/L$ ) in channel #2.

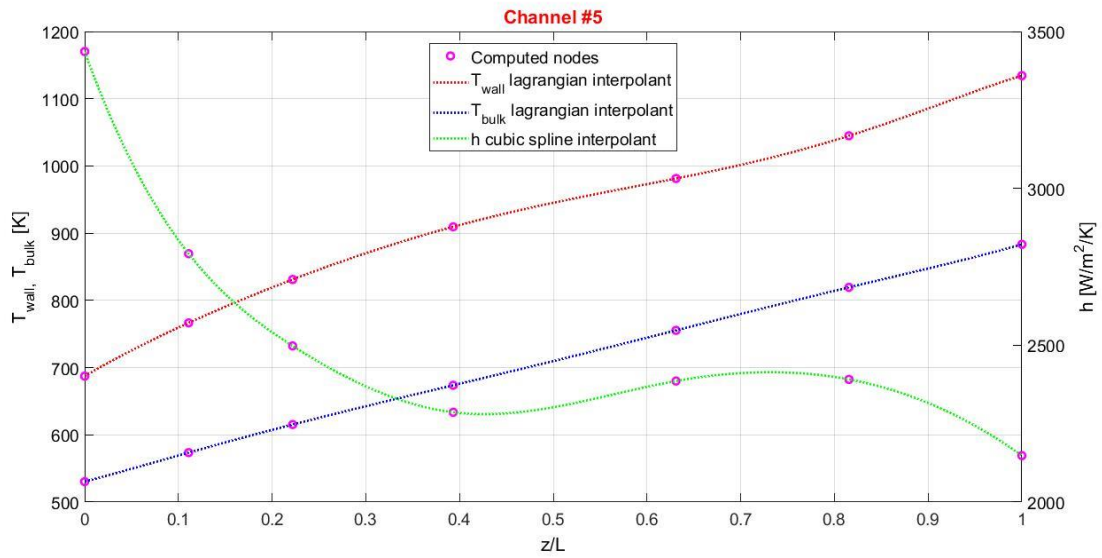


Figure 5.22: Computed nodes and interpolant functions for wall temperature ( $T_{wall}$ ), mass flow averaged temperature ( $T_{bulk}$ ) and heat transfer coefficient ( $h$ ) as a function of normalized axial distance ( $z/L$ ) in channel #5.

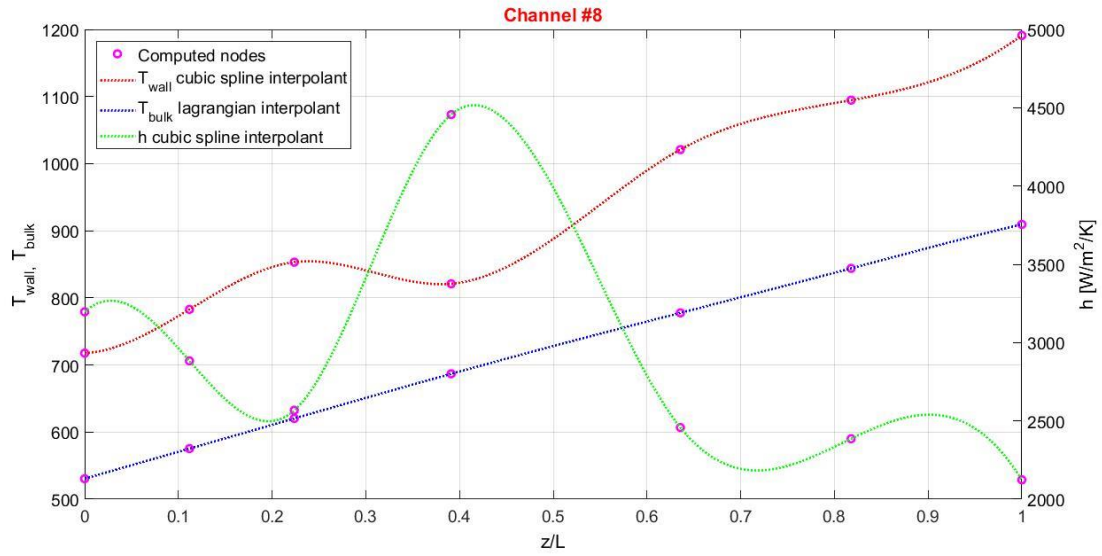


Figure 5.23: Computed nodes and interpolant functions for wall temperature ( $T_{wall}$ ), mass flow averaged temperature ( $T_{bulk}$ ) and heat transfer coefficient ( $h$ ) as a function of normalized axial distance ( $z/L$ ) in channel #8.

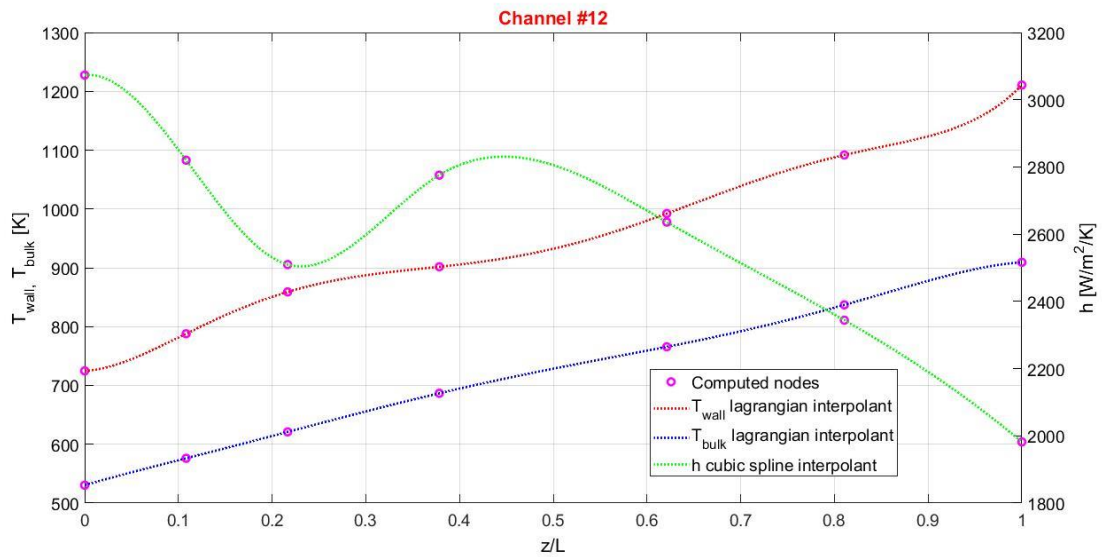
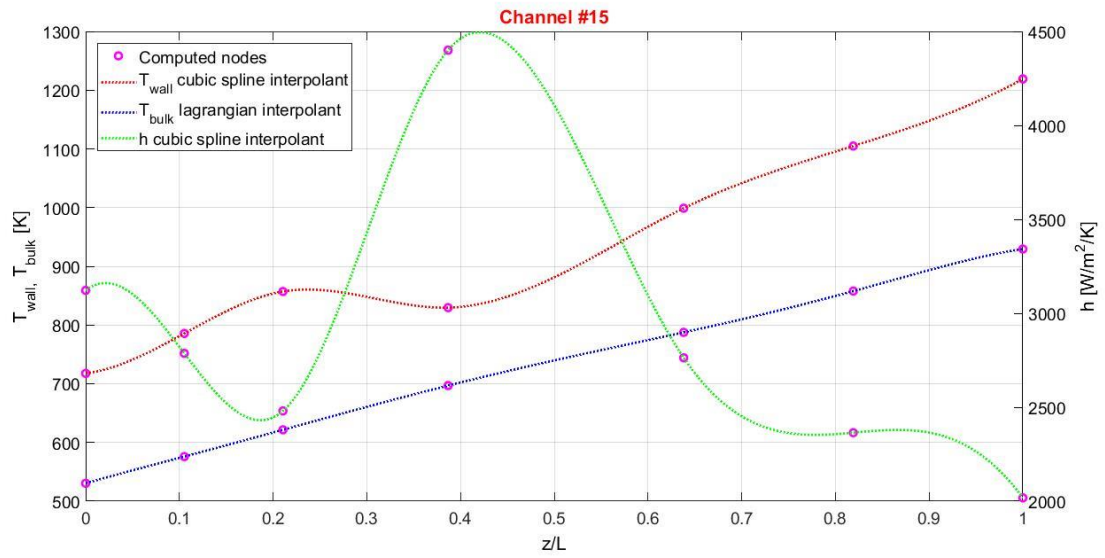


Figure 5.24: Computed nodes and interpolant functions for wall temperature ( $T_{wall}$ ), mass flow averaged temperature ( $T_{bulk}$ ) and heat transfer coefficient ( $h$ ) as a function of normalized axial distance ( $z/L$ ) in channel #12.



**Figure 5.25:** Computed nodes and interpolant functions for wall temperature ( $T_{wall}$ ), mass flow averaged temperature ( $T_{bulk}$ ) and heat transfer coefficient ( $h$ ) as a function of normalized axial distance ( $z/L$ ) in channel #15.

## 6. Second Case Study: Ceramic Core Insert

Second part of the present study is focused on analysis of modified TG20 row 1 blade cooling system. Z shaped channels are no longer present and fifteen straight channels are filled with air that comes from a chamber, in which air mixing takes place.

As showed in present chapter, this geometry presents some criticalities regarding air flow dynamic in the mixing zone which affect cooling effectiveness: considering limitations of *PH4165* software, CFD analysis was the only way to highlight these problems. Computational Fluid Dynamic analysis is, as for the present study, a fundamental tool in order to have a complete description of the phenomenon, which in many cases is not provided by other software.

### 6.1 Thermal Fluid Dynamic Analysis: Criticalities of the system

Object of the second part of the present study is the domain showed in [Figure 6.1](#): as it can be noticed, air is flowing trough two large channels, which are called *manifolds*, then in *chamber* region air mixing takes place, finally air gets inside fifteen straight ducts, cooling down metal parts that are directly facing hot gases from combustion chamber. Even in this case, inlet and outlet chambers are present, in order to properly impose total pressure boundary. Boundary conditions are resumed in following tables: heat source value was derived from *PH4165* software data: aim of this analysis was to validate mass flow and bulk outlet temperature of each channel, as it has been made for old geometry analysis.



*Figure 6.1: Air domain in new cooling system CFD analysis.*

INLET MANIFOLD #		
	1	2
$p_{static,inlet}$ [bar]	18.00	18.00
$p_{total,inlet}$ [bar]	9.34	9.34
$T_{total,inlet}$ [K]	499.44	499.44
$Q_{ANIMA}$ [kW]	6.992	

**Table 6.1:** Boundary conditions of inlet manifolds surfaces in currently adopted geometry CFD analysis: it can be noticed that heat source is imposed in both manifold and chamber region.

CHANNELS #															
	1	2	3	4	5	6	7	8	9	10	11	12	13	14	15
$p_{total,outlet}$ [bar]	6.38	6.38	6.38	5.89	5.89	5.89	5.40	5.40	5.40	4.90	4.90	4.90	4.90	4.90	4.90
$T_{total,outlet}$ [K]	728.89	728.89	728.89	830.00	830.00	830.00	855.56	855.56	855.56	855.56	855.56	855.56	855.56	855.56	855.56
$Q_{channel}$ [kW]	0.158	0.158	0.158	0.236	0.236	0.236	0.284	0.284	0.284	0.284	0.284	0.284	0.284	0.284	0.284
	GROUP 1			GROUP 2			GROUP 3			GROUP 4					

**Table 6.2:** Boundary conditions of outlet channels surfaces in currently adopted geometry CFD analysis.

Same physical models and solvers of the *radial holes* analysis have been used for the present simulation. Number of channel layers have been reduced in order to maintain constant cell aspect ratio in channels region. In *ANIMA* region (both entry manifolds and mixing chamber) a base size of 0.35 mm has been adopted, and number of prism layers is 4. Total number of cells is equal to 2'609'135.

As in showed in following figures, the present cooling geometry is suffering of stagnation in two zones, both located in the mixing chamber. In these areas, air flow velocity is almost null: combination of this condition with heat source boundary, determines wall temperature to reach maximum temperature allowable according to the software, which is 5000 K.

This means that it is not possible to study thermal response of the system according to company data: wall temperature boundary condition would be the preferred one for this geometry, but this is unknown unless the complete conjugated heat transfer problem is solved.

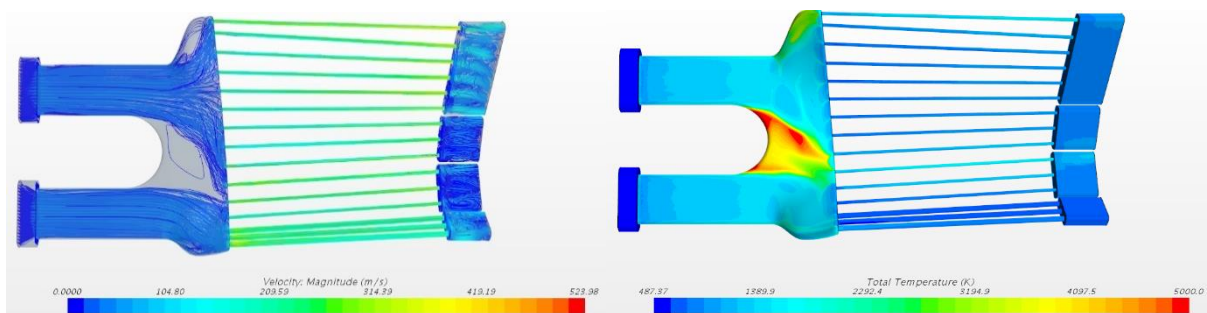


**Figure 6.2:** Velocity streamlines (left) and wall total temperature (right) maps for currently adopted cooling system: it can be noticed that hot spot arises where stagnation takes place.

## 6.2 Segregated Isothermal Analysis

In order to have at least a description of air flow dynamic inside this cooling path, a new approach has been considered: air flow is supposed as isothermal, with total temperature equal to air inlet temperature according to *PH4165* software. Due to the fact that energy equation is no more solved, physic model was changed from coupled approach to segregated one. Still unsteady problem is solved, with time-step of 5E-06 s and total transient duration of 0.015 s. Except for total temperature, which is fixed to 499.44 K, initial and boundary conditions are unchanged. No heat source is imposed in any part of the region.

Aim of this analysis is to highlight criticalities of “cold” air flow, in order to see if some channels are penalized in term of mass flow, or if other zones are experiencing stagnation.

Even in this case, grid independence analysis has been made, in order to estimate error content related to domain discretization.

### 6.2.1 ANIMA Region Base Size Sensitive Analysis

In order to estimate error related to *ANIMA* region, sensitive analysis on base size has been made. Meshing conditions in control volumes regions are unchanged with respect to fifteen channels geometry. Channels base size and prism layers are unchanged, and number of channel layers has been reduced from 500 to 258: this was made in order to keep constant cell aspect ratio in that region.

For *ANIMA* region, selected number of prism layers is 4: this choice was made according to previous sensitive analysis, but it is worth to have future studies on this. Three different mesh size were tested: results are reported in following table. Linear error decrease hasn't been reached for many physical parameters so, in the end, selected mesh size was 0.70 mm due to impossibility to estimate error related to 0.35 mm base size mesh.

		INLET SECTION 1		CHANNEL #2				
base size [mm]	# of region cells	$\dot{m}_{in}$ [g/s]	$p_{in}$ [bar]	$\dot{m}_{in}$ [g/s]	$p_{in}$ [bar]	$\dot{m}_{out}$ [g/s]	$p_{out}$ [bar]	$\Delta p$ [bar]
1.4	164757	18.450	9.37	4.662	10.06	4.914	8.63	1.42
0.7	410878	18.310	9.39	4.689	10.05	4.896	8.63	1.41
0.35	906476	18.931	9.40	4.715	10.05	4.975	8.58	1.47

*Table 6.3: Grid independence analysis results for ANIMA region base size; highlighted line is the chosen base size.*

In this way, total discretization error for each of the monitor of interest, can be estimated as superposition between discretization error related to channels region, which has been reduced with respect to previous case, and discretization error related to *ANIMA* region. Total relative error for each monitor are almost the same order of magnitude with respect to *radial holes* simulation. Following figure is showing the adopted mesh: total number of cells is equal to 2'169'330.

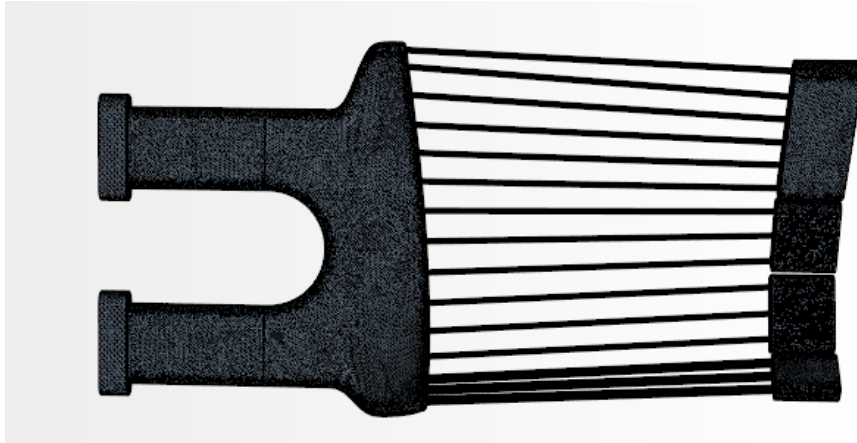


*Figure 6.3: Scene of the adopted mesh for new cooling geometry analysis.*

### 6.2.2 Final Results and New Possible Design

All these results are from simulation with selected mesh according to grid independence analysis. Simulation reached convergence, all residuals are below threshold value, except for turbulent dissipation rate ( $\epsilon$ ) residual: cells that tdr value is above threshold one are again located in channels region but, as in the case of *radial holes* simulation, this must be accepted unless a mesh refinement is considered, regarding that it may cause CPU troubles.

According to monitors results, none of the fifteen channels is characterized by reduced mass flow with respect to the others so flow distribution is homogeneous along this portion of the domain. On the other hand, fluid flow is non-homogeneous in *ANIMA* region and still same two stagnation zones are present: one just before air expansion from manifolds to the chamber and the other one in then 15<sup>th</sup> channel entry zone. Stagnation can be considered as a feature of this cooling geometry and new design should be considered: as a matter of fact, even if channels effectiveness seems unchanged, also cooling in root region is something that is necessary to take care when designing gas turbine blade.

Channels #		$\dot{m}_{in}$ [g/s]		$\dot{m}_{out}$ [g/s]		$p_{in}$ [bar]		$p_{out}$ [bar]		$\Delta p$ [bar]	
		Computed	Uncertainty	Computed	Uncertainty	Computed	Uncertainty	Computed	Uncertainty	Computed	Uncertainty
GROUP 1	1	4.773	$\pm 0.130$	4.965	$\pm 0.149$	10.04	$\pm 0.04$	8.57	$\pm 0.07$	1.47	$\pm 0.09$
	2	4.715	$\pm 0.128$	4.942	$\pm 0.149$	10.05	$\pm 0.04$	8.60	$\pm 0.07$	1.44	$\pm 0.09$
	3	4.588	$\pm 0.125$	4.929	$\pm 0.148$	10.05	$\pm 0.04$	8.60	$\pm 0.07$	1.45	$\pm 0.09$
GROUP 2	4	1.602	$\pm 0.044$	1.808	$\pm 0.054$	9.97	$\pm 0.04$	8.12	$\pm 0.07$	1.85	$\pm 0.12$
	5	1.582	$\pm 0.043$	1.797	$\pm 0.054$	9.94	$\pm 0.04$	8.11	$\pm 0.07$	1.82	$\pm 0.11$
	6	1.557	$\pm 0.042$	1.774	$\pm 0.053$	9.94	$\pm 0.04$	8.05	$\pm 0.07$	1.88	$\pm 0.12$
GROUP 3	7	1.628	$\pm 0.044$	1.859	$\pm 0.056$	9.93	$\pm 0.04$	7.89	$\pm 0.07$	2.04	$\pm 0.13$
	8	1.638	$\pm 0.045$	1.869	$\pm 0.056$	9.96	$\pm 0.04$	7.92	$\pm 0.07$	2.04	$\pm 0.13$
	9	1.644	$\pm 0.045$	1.872	$\pm 0.056$	9.97	$\pm 0.04$	7.90	$\pm 0.07$	2.07	$\pm 0.13$
GROUP 4	10	1.659	$\pm 0.045$	1.892	$\pm 0.057$	9.96	$\pm 0.04$	7.65	$\pm 0.06$	2.31	$\pm 0.14$
	11	1.655	$\pm 0.045$	1.887	$\pm 0.057$	9.94	$\pm 0.04$	7.64	$\pm 0.06$	2.30	$\pm 0.14$
	12	1.662	$\pm 0.045$	1.892	$\pm 0.057$	9.94	$\pm 0.04$	7.66	$\pm 0.06$	2.29	$\pm 0.14$
	13	1.666	$\pm 0.045$	1.879	$\pm 0.056$	9.96	$\pm 0.04$	7.64	$\pm 0.06$	2.32	$\pm 0.15$
	14	1.655	$\pm 0.045$	1.866	$\pm 0.056$	9.94	$\pm 0.04$	7.59	$\pm 0.06$	2.35	$\pm 0.15$
	15	1.645	$\pm 0.045$	1.853	$\pm 0.056$	9.95	$\pm 0.04$	7.57	$\pm 0.06$	2.38	$\pm 0.15$

*Table 6.4: Monitor results and their relative uncertainty, as a result of new cooling geometry analysis.*

Efficient root cooling is necessary in order to decrease maximum stress value, which is usually located in dovetail joint; another benefit is that, with efficient root cooling, blades acts as a fin with respect to the disc, decreasing its working temperature with consequent advantages regarding fatigue resistance.

According to simulations results, a new design for ceramic insert should be considered, here are some possible solutions:

- Ceramic core reshaping, allowing sudden geometry variation and guide air also trough zones that are suffering of stagnation;
- Increasing number of inlet manifolds from two to three, and reshaping them to keep constant total resistant area of the blade in each cross section, in this way, each of the fifteen channels would be properly filled with air and at the same time a homogeneous flow field would be ensured;
- Addition of v-shaped ribs, in order to both guide air trough stagnation zones and increase turbulence of the flow field with low pressure drop due to relatively low velocity magnitude.

## 7. Conclusions

### 7.1 Summarizing Conclusions

Objects of the present work are Computational Fluid Dynamic (CFD) analysis of air-cooling flow in a heavy industrial gas turbine blade. These analyses have been carried on in order to validate results from flow network solver software. First group of analyses were focused on *radial hole* cooling geometry: starting from simple channels, it has been carried out a complete sensitive analysis on the base size, showing consistency of the model. Result of this study is that most accurate mesh for our case study is a structured one, with elongation in “wind” direction and polyhedral base size. Linear error decrease has been reached for all parameters of interest, giving us the chance to have very accurate error control connected to domain discretization.

First group analysis showed that, for more complex geometry, transient analysis must be preferred with respect to the steady state because of its stability without any numerical control, as well as a faster convergence. It gave us also the possibility to show the effect of common inlet control volume for more than just one channel and how this is affecting air behaviour.

Although increased uncertainty because of higher convergence error, results from fifteen channels geometry are quite promising. This analysis provides a complete description of cooling mechanism inside *TG20* turbine blade: a complete comparison between CFD model and *PH4165* software was derived is showed in [Table 7.1](#).

Monitors matching are quite good for large diameter channels, but percentage differences between CFD and air flow network software reaches 20% for mass flow monitor in case of channels with small diameters: this can be explained considering that control volumes that are present in CFD analysis determine local pressure drops, reducing air momentum. Generally speaking, it is possible to say that *PH4165* provides good channels modelling in term of air dynamic. Regarding heat transfer coefficient, the average one estimated by *Ethos* engineers was smaller with respect to one computed by *Star-CCM+*; moreover, thanks to CFD tool, it was possible to have local map of convective heat transfer coefficient ( $h$ ) all along each channel.

Currently adopted geometry analysis was a great example of how much CFD analysis can be important in order to appreciate phenomenon that happens in a little portion of the blade but

may affects operating conditions of the entire gas turbine. Cooling criticalities raised during these simulations: new ceramic core insert is suffering of stagnation in many zones, which means a proper heat transfer coefficient is not ensured in root region of the blade, where typically maximum stress is present. Stagnation makes unfeasible to study heat transfer mechanism when applying heat source boundary condition, so just air fluid dynamic was object of these analysis. It was showed that, although air flow field in ceramic core insert is non-uniform, none of the fifteen channels is experiencing a reduced mass flow, and cooling effectiveness in air foil region of the blade is expected to be unchanged. As a conclusion, we can say that *PH4165* model is unfeasible for this complex geometry, and more powerful tools are needed to fully understand air behaviour inside ceramic insert.

channels #	$\dot{m}_{in}$ [g/s]		$\dot{m}_{out}$ [g/s]		$p_{in}$ [bar]		$p_{out}$ [bar]		$\Delta p$ [bar]		$T_{bulk}$ [K]		
	CFD	PH4165	CFD	PH4165	CFD	PH4165	CFD	PH4165	CFD	PH4165	CFD	PH4165	
GROUP 1	1	3.697	3.882	3.655	3.882	9.17	9.55	7.41	6.38	1.76	3.17	741.44	728.89
	2	3.790	3.882	3.742	3.882	9.15	9.55	7.41	6.38	1.73	3.17	737.06	728.89
	3	3.848	3.882	3.802	3.882	9.15	9.55	7.49	6.38	1.67	3.17	734.11	728.89
GROUP 2	4	1.257	1.509	1.242	1.509	9.26	9.55	6.96	5.89	2.30	3.66	888.87	830.00
	5	1.278	1.509	1.261	1.509	9.24	9.55	7.01	5.89	2.23	3.66	883.39	830.00
	6	1.257	1.509	1.246	1.509	9.26	9.55	7.00	5.89	2.26	3.66	887.53	830.00
GROUP 3	7	1.289	1.512	1.279	1.512	9.24	9.55	6.69	5.40	2.55	4.15	907.76	855.56
	8	1.284	1.512	1.271	1.512	9.24	9.55	6.69	5.40	2.55	4.15	909.50	855.56
	9	1.291	1.512	1.278	1.512	9.23	9.55	6.69	5.40	2.55	4.15	907.46	855.56
GROUP 4	10	1.329	1.568	1.315	1.568	9.22	9.55	6.45	4.90	2.77	4.65	911.00	855.56
	11	1.341	1.568	1.325	1.568	9.21	9.55	6.50	4.90	2.71	4.65	907.47	855.56
	12	1.333	1.568	1.318	1.568	9.21	9.55	6.47	4.90	2.74	4.65	909.40	855.56
	13	1.317	1.568	1.300	1.568	9.22	9.55	6.41	4.90	2.81	4.65	915.03	855.56
	14	1.294	1.568	1.276	1.568	9.24	9.55	6.36	4.90	2.88	4.65	921.30	855.56
	15	1.266	1.568	1.248	1.568	9.25	9.55	6.35	4.90	2.90	4.65	929.52	855.56

Table 7.1: Monitors comparison between CFD 15 channels analysis and PH4165 software.

## 7.2 Future Studies

CFD analysis was just first step of a very complex study, which is description of thermo-mechanical response of *TG20* gas turbine blade under the action of hot gases and centrifugal force. Local heat transfer map for *radial holes* may be a fundamental input for a FEM analysis of the blade, in order to have local map of stress and strain in the structure.

Regarding the cooling geometry with ceramic core insert, a more complete sensitive analysis concerning mesh size is advisable; then, alternative boundary condition with respect to imposed heat source is needed in order to study thermal response of the system. A possible approach could be solution of conjugated heat transfer problem, but this may require high computational

resource, so other options should be taken into account. Then, new ceramic insert outline is advisable, some possible solutions have been presented in [Chapter 6](#): main feature of this design should be absence of stagnation zones, and adoption of technologies for air turbulence enhancing, with consequent heat transfer increase in root blade region.

Other possible future studies may involve more complex cooling systems, like adoption of ribbed channels, in order to further increase turbulence of air flow, or film formation around air foil, in order to reduce blade wall temperature at hot gas interface.

*TG20* is characterized by lower efficiency with respect to competitor machine of the same size: thus, under a wider perception, *EthosEnergy* engineers should consider general redesign, in order to be more competitive in the heavy industrial gas turbine sector. A new, complete and more accurate map of secondary flow is needed, using more efficient tools for air flow network analysis: this would give the chance to better estimate first rotor disc fatigue resistance and understand why this component is suffering of creep, which is the main failure mode of the turbine.

## Bibliography

1. International Energy Agency  
*World Energy Outlook 2018* (<https://www.iea.org/weo2018/>) - 2018
2. The Global Journal of Energy Equipment  
*Worldwide Gas Turbine Forecast* (<https://www.turbomachinerymag.com/worldwide-gas-turbine-forecast-2/>) – 11/15/2018
3. M.P. Boyce  
*Gas Turbine Engineering Handbook (4<sup>th</sup> edition)* – Butterworth Heinemann, 2012
4. A. Poggio  
*Appunti di Fondamenti di Macchine – academic year 2015/2016*
5. B. Lakshminarayana  
*Fluid Dynamics and Heat transfer of Turbomachinery – John Wiley & Sons, 1995*
6. J. Town, D. Straub, J. Black, K.A. Thole, T.I.P. Smith  
*State-of-the-Art Cooling Technology for a Turbine Rotor Blade – Journal of Turbomachinery (copyright by ASME), 07/2018*
7. J. Sundberg  
*Heat Transfer Correlations for Gas Turbine Cooling – 2006*
8. S. Gupta<sup>1</sup>, A. Chaube<sup>1</sup> and P. Verma  
*Review on Heat Transfer Augmentation Techniques: Application in Gas Turbine Blade Internal Cooling – Journal of Engineering Science and Technology Review, Accepted 10/06/2012*
9. B.R. Munson, T.H. Okiishi, W.W. Huebsch, A.P. Rothmayer  
*Fluid Mechanics – John Wiley & Sons, 2010*
10. A. Bakker  
*Course material for Computation Fluid Dynamic Class at Dartmouth College* (<http://www.bakker.org/dartmouth06/engs150/>) – 2002
11. J.H. Ferziger, M. Peric  
*Computational Methods for Fluid Dynamics (3<sup>rd</sup> edition)* – Springer-Verlag, 2002
12. D.C. Wilcox  
*Turbulence Modeling for CFD (3<sup>rd</sup> edition)* – DWC Industries, 2006
13. A. Quarteroni, F. Saleri, P. Gervasio  
*Scientific Computing with MATLAB and OCTAVE (4<sup>th</sup> edition)* – Springer-Verlag, 2014

## Acknowledgement

*“The world I love  
The tears I drop  
To be part of  
The wave, can't stop  
Ever wonder if it's all for you?”*

– *Red Hot Chili Peppers*

Voglio dedicare questo spazio alle persone importanti della mia vita, per ricordare loro e me stesso che bene prezioso sono: senza di voi nulla di questo sarebbe stato possibile.

Ai miei genitori Fabio e Barbara, la mia fortuna più grande, a voi va tutto il merito per quello che sono oggi. Con la volontà di rendervi sempre orgogliosi, in segno della mia immensa riconoscenza.

A Fefo: hermano, amigo y complice del delito. Chitarrista molesto, discreto coinquilino ma migliore fratello del mondo.

Ai nonni Geni e Ninì, sostenitori economici e culinari di questo ambizioso progetto chiamato laurea in Ingegneria.

A Leon, massa informe di peli da cui si affacciano due occhi dolcissimi. Fidato ascoltatore nei momenti di maggiore sconforto.

A tutta la mia famiglia: zia Bruna, Fausta e Marco, zia Maria, la prof. Floriana, Fabri e Marco, zia Liliana e zio Paolo e sicuramente scorderò qualcuno ma siete tutti un tassello importante del mio cuore.

A tutti i componenti di Orgiameli e Fantastici 5, compagni e amici di vita. Mancate cornutazzi! Non potrei mai dimenticarmi di Bobo, uomo di altri tempi e fidato compagno di studi, a te devo parte dell'ingegnere che sarò.

A Bibi, che vuole solo il meglio per me. Con l'impegno di proteggere per sempre la grazia del tuo cuore. Orgoglioso di essere parte della tua vita.

A tutti voi, GRAZIE!

